Bulletin of the Seismological Society of America, Vol. 107, No. 5, pp. 2225–2246, October 2017, doi: 10.1785/0120170017

Ⓔ

New Empirical Earthquake Source-Scaling Laws

by Kiran Kumar S. Thingbaijam, P. Martin Mai, and Katsuichiro Goda

Abstract We develop new empirical scaling laws for rupture width W, rupture length L, rupture area A, and average slip D, based on a large database of rupture models. The database incorporates recent earthquake source models in a wide magnitude range (M_w 5.4–9.2) and events of various faulting styles. We apply general orthogonal regression, instead of ordinary least-squares regression, to account for measurement errors of all variables and to obtain mutually self-consistent relationships.

We observe that L grows more rapidly with M_w compared to W. The fault-aspect ratio (L/W) tends to increase with fault dip, which generally increases from reverse-faulting, to normal-faulting, to strike-slip events. At the same time, subduction-interface earthquakes have significantly higher W (hence a larger rupture area A) compared to other faulting regimes. For strike-slip events, the growth of W with M_w is strongly inhibited, whereas the scaling of L agrees with the L-model behavior (D correlated with L). However, at a regional scale for which seismogenic depth is essentially fixed, the scaling behavior corresponds to the W model (D not correlated with L). Self-similar scaling behavior with $M_w - \log_{10} A$ is observed to be consistent for all the cases, except for normal-faulting events. Interestingly, the ratio D/W (a proxy for average stress drop) tends to increase with M_w, except for shallow crustal reverse-faulting events, suggesting the possibility of scale-dependent stress drop.

The observed variations in source-scaling properties for different faulting regimes can be interpreted in terms of geological and seismological factors. We find substantial differences between our new scaling relationships and those of previous studies. Therefore, our study provides critical updates on source-scaling relations needed in seismic–tsunami-hazard analysis and engineering applications.

Electronic Supplement: Figures depicting regression analysis, normality probability plots, and comparisons between different source-scaling relationships; and tables listing rupture models and different earthquake source-scaling relationships.

Introduction

Earthquake source-scaling relations provide empirical equations that link observable source parameters to each other. Such scaling relations not only provide insight into earthquake mechanics (e.g., Scholz, 1982; Romanowicz, 1992; Wells and Coppersmith, 1994; Mai and Beroza, 2000; Blaser *et al.*, 2010; Skarlatoudis *et al.*, 2016) but also constitute an essential ingredient in seismic–tsunami-hazard studies (e.g., Stafford, 2014; De Risi and Goda, 2016). However, available databases are limited, whereas uncertainties in the source parameters (primarily rupture length L, rupture width W, average displacement D, and seismic moment M_0) are hardly considered. Our study tries to partially overcome these limitations using the database of finite-fault source models (Mai and Thingbaijam, 2014) that spans a wide magnitude range (M_w 5.4–9.2) and also provides multiple estimates of source parameters for a large number of events that have been studied by different research groups. In addition, for a set of earthquakes, information on fault segmentation is available that has not been included so far in any source-scaling analysis.

Several studies investigated earthquake source-scaling properties (for a summary, see Stirling *et al.*, 2013); however, most of them employed datasets not limited to rupture models but based on indirect estimates of source parameters (e.g., early aftershocks) and surface-rupture observations that are prone to large uncertainties. Using only rupture models for which the uncertainties in source parameters can be consistently inferred, we strive for a more objective assessment of the source-scaling properties.

The inversions for rupture models using either seismic recordings, geodetic data, or both determine the spatiotemporal properties of the rupture processes. Therefore, the cor-

responding source dimensions L, W, and A, as well as the seismic moment M_0, are more-accurately and self-consistently estimated than from aftershock zones and/or surface ruptures. Earlier investigations of source-scaling properties based exclusively on rupture models lacked very large magnitude events (e.g., Somerville *et al.*, 1999; Mai and Beroza, 2000). Other studies focused on region-specific scaling relationships (Murotani *et al.*, 2008; Yen and Ma, 2011; Rodríguez-Pérez and Ottemöller, 2013; Ramírez-Gaytán *et al.*, 2014) or a specific fault regime, like subduction events (Murotani *et al.*, 2013; Skarlatoudis *et al.*, 2016; Ye *et al.*, 2016). Thus, there is a need to reexamine earthquake source-scaling properties using a global set of rupture models, considering different faulting regimes and including very large and megathrust events. Such a study is now feasible because of the increased availability of inverted kinematic source models for past earthquakes.

We emphasize that regression analyses between the different source parameters should produce empirical scaling laws that are fundamentally self-consistent. As explained by Leonard (2010), the self-consistency implies that the scaling equations between different parameters mutually agree with each other, as well as with the definition of seismic moment. Another requirement is that the scaling relationship remains invariant under an interchange of variables; for instance, the relationship between magnitude and rupture length should be the same, irrespective of which of the two parameters is the independent or dependent variable. This condition can be met by enforcing theoretical expectations on the scaling coefficients (e.g., the slope of a linear model) in the regression analysis (e.g., Somerville *et al.*, 1999; Hanks and Bakun, 2002; Leonard, 2010). However, in the present study, we make no such prior assumptions regarding the scaling coefficients in order to let the data speak, not theoretical expectations. Instead, we attempt to improve the regression analysis considering errors-in-variables models by applying general orthogonal regression (GOR). Thus, the self-consistency of the scaling laws developed in this study is data driven with no prior assumptions about the relationships.

In the following sections, we describe the finite-fault rupture-model database, our approach to the data selection, classification, and preprocessing, the regression technique, and then we present the new empirical scaling laws for the earthquake source. To develop the scaling laws, we compute the specific source parameters from the rupture models, and then apply regression analysis on the resulting data. More specifically, we first address the scaling properties of rupture dimensions, considering different faulting regimes, and compare our results with previous studies. Next, we examine the implications, immediate conclusions, and physical interpretations relevant to rupture dynamics from the new relationships and discuss their practical aspects.

Finite-Fault Rupture Models

The present study is motivated by the recently augmented online repository of kinematic earthquake-rupture models, the SRCMOD database (Mai and Thingbaijam, 2014). This database embodies the recent surge in finite-fault source-inversion studies of earthquakes. For discussions on the different data and inversion techniques used to develop these rupture models, we refer the readers to Mai and Thingbaijam (2014). The SRCMOD database comprises the current largest online repository of rupture models for past global earthquakes, organized in a uniform and consistent manner.

It is important to note that appreciable uncertainties exist with these rupture models, owing to the ill-posed nature of earthquake-source inversions because of limited and nonuniform data coverage, incompletely known crustal structure, and unknown errors in data and modeling assumptions (Beresnev, 2003; Mai *et al.*, 2007, 2016). Nevertheless, these rupture models were obtained by applying known physics of seismic-wave excitation and propagation and/or crustal deformation due to earthquake slip. Thus, these rupture models represent the currently best-resolved attributes of kinematic earthquake-source properties and have been extensively used to investigate the rupture physics (for reviews on this aspect, see e.g., Mai and Thingbaijam, 2014; Thingbaijam and Mai, 2016). Varying techniques and data applied by different research teams to study the same event introduce intraevent variability into the rupture models, but they also minimize possible bias due to inversion techniques or to the data used for the source inversion. Thus, multiple rupture models for the same event allow accounting for independent (and usually different) source-parameter estimates.

Before we describe our approach for selecting rupture models for the analysis, we briefly discuss the relevant features of a rupture model. A rupture model usually comprises several kinematic source parameters: slip, rise time (duration of slip), rupture-onset time, and rake (angle of slip direction) assigned at node points (or subfaults) on the rupture plane(s). In the present study, we are concerned only with the final displacement over the fault plane, that is, the slip distribution, whereas the temporal rupture evolution is neglected. The spatial extent of the slip distribution along-strike and down-dip is related to the rupture length and rupture width. The size of the subfaults, that is, the spacing of the node points with respect to the rupture area, defines a nominal spatial resolution of the model. Owing to the chosen spatial discretization in the source inversion and the need to utilize bandlimited data, rupture models do not account for small-scale fault-surface roughness (occurring on a 1–100 m scale) but incorporate large-scale fault segmentations (occurring on a scale of several kilometers).

Data Selection and Classification

The spatial resolution of rupture models largely decides whether or not the application of a specific statistical analysis will be statistically meaningful. Accordingly, we apply the following criteria to examine the suitability of the rupture models:

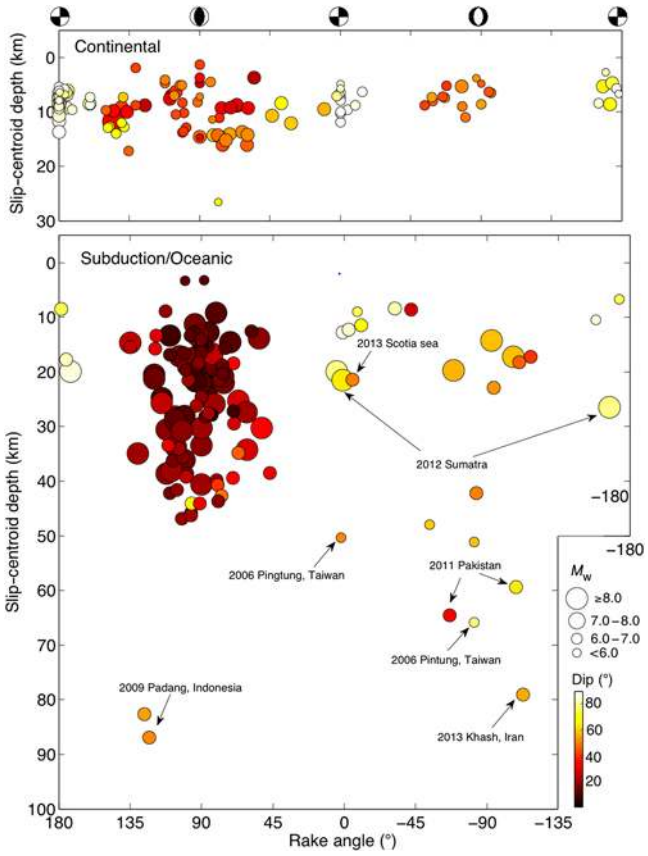

Figure 1. The distribution of slip-centroid depth, average rake angles, average fault dip, and magnitudes in the present dataset. The plots include, if available, multiple models for the same event. Two models for the 2013 Okhotsk Sea earthquake, a shallow-dip normal-faulting event with slip-centroid depth > 600 km are not depicted. A few exceptional events are annotated. The color version of this figure is available only in the electronic edition.

1. a magnitude $M_w \geq 5.0$, because smaller events are likely to be less well resolved in the inversions;
2. the number of subfaults in down-dip or along-strike are larger than three to allow computing effective source dimensions (see the Data Processing section); and
3. when, for the same event, multiple rupture models are produced by the same author(s), we use its latest version.

Figure 1 depicts the distributions of the selected rupture models in terms of slip-centroid depth, fault-dip, and average rake angles. We use the centroid depth of the slip distribution (as a measure of effective rupture depth) to overcome the lack of hypocentral locations in inversions of geodetic data. This initial selection comprises 268 rupture models from 142 earthquakes that we further examine in terms of different faulting regimes.

Earthquake source-scaling properties are found to depend on the seismotectonic regime and faulting style (see Stirling *et al.*, 2013). Therefore, we group rupture models according to the faulting styles. We broadly classify seismotectonic regimes as either continental, oceanic, or subduction zones.

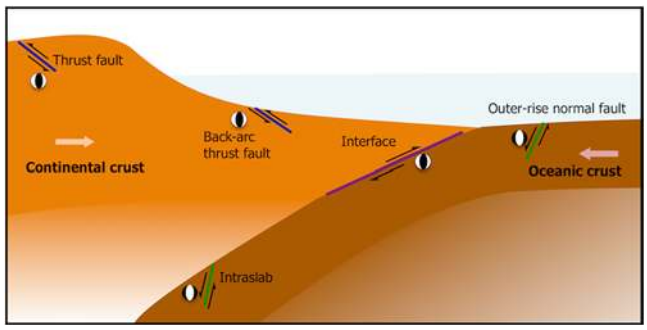

Figure 2. A schematic diagram depicting different dip-slip regimes in a oceanic–continental subduction-collision zone. These dip-slip regimes differ from each other in terms of associated active tectonic loading and material properties. The color version of this figure is available only in the electronic edition.

Figure 1 shows that the tectonic regime largely controls the distributions of rupture depth and fault dip. For continental earthquakes, the slip centroids are well confined within a depth of 20 km. On the other hand, earthquakes in subduction zones can occur at significant depths. Subduction-interface events occur within a depth of 50 km, whereas intraslab (or in-slab) events can be observed at depths over 100 km. Furthermore, we find that the average fault-dip angles δ are correlated with average rake angles, transitioning from steeper to shallower from strike-slip ($\delta \sim 70°$–$90°$) to normal-faulting ($\delta \sim 50°$–$60°$) to shallow crustal reverse-faulting ($\delta \sim 40°$–$50°$) and finally to subduction-interface ($\delta \sim 10°$–$30°$) events.

In continental and oceanic crust, earthquakes occur within the tectonic plate (intraplate) or at the interface between two tectonic plates (interplate). Intraplate events can be located either at the margins or interiors of the tectonic plates (Scholz *et al.*, 1986). In the present dataset, intraplate events at active plate margins, mostly those in western North America and inland Japan, dominate the continental reverse-faulting events. The source-scaling properties of events in stable continental regions (SCRs) are reported to be different from interplate as well as intraplate events (e.g., Johnston and Kanter, 1990; Leonard, 2014). However, we have only six events associated with SCR and therefore exclude SCR events from our analysis.

For reverse-faulting earthquakes, we distinguish between shallow crustal and subduction-interface events. We classify the 2015 Gorkha earthquake as a continental subduction event, owing to its rupture characteristics (e.g., Goda *et al.*, 2016). Figure 2 illustrates the different dip-slip regimes in an oceanic–continental subduction zone. These include continental, back-arc and subduction-interface thrust faults, and outer-rise and subduction in-slab normal faults. They differ from each other in terms of their associated tectonic loading mechanisms, as well as in the dominating material properties. For the analysis, we do not differentiate continental and shallow back-arc thrust faulting but group them as reverse-faulting (shallow crustal) events. However,

we analyze the subduction-interface events separately. Owing to limited data, we examine outer-rise and in-slab normal-faulting events jointly, although outer-rise events occur at shallower regions and have different tectonic settings than subduction in-slab events that occur within the dipping plate at larger depths.

We define the dominant faulting types, such as strike slip, normal, reverse, or oblique slip, based on average rake angle. Because considerable spatial variability of rake angles across a rupture plane may occur, we adopt a slip-weighted average rake angle

$$\lambda_{\text{avg}} = \frac{\sum u_i \lambda_i}{\sum u_i}, \qquad u_i \geq \frac{1}{3} u_{\max}, \tag{1}$$

in which u and $u_{\max}$ refer to slip and maximum slip on the rupture plane, respectively. The stipulated range of slip corresponds to large-slip asperities (Mai *et al.*, 2005) and limits the computation for the slip type to prominent parts of the rupture.

Figure 1 indicates considerable variability of rake angles in our database. In many cases, clusters are observed that can be attributed to multiple models for the same events. For instance, continental events with average rake angles between 130° and 150° amount to only six earthquakes but 16 rupture models altogether. We examine whether oblique-slip events exhibit any characteristic scaling properties. First, we apply an optimal case with bin size of 15° and with rake angle centered at 0°, −180° for strike-slip, 90° for reverse-faulting, and −90° for normal-faulting events, thus clearly separating oblique-slip events. Then, we assess oblique-slip events in terms of data scattering with respect to these three faulting types. Overall, the data scatter does not support characteristic scaling of oblique-slip events.

Therefore, we classify the oblique-slip events into either one of the three faulting types but do not analyze them specifically. Only three events with very atypical rupture dimensions (for their dominant faulting type) are examined separately, namely, the 1978 $M_w \sim 7.1$ Tabas (one source model), the 1989 $M_w \sim 6.9$ Loma Prieta (five source models), and the 2008 $M_w \sim 7.9$ Wenchuan (four source models) earthquakes. These events are characterized by strongly oblique slip, comprising reverse dip slip with considerable strike-slip components.

In summary, we classify the earthquakes into four broad categories based on the faulting regimes. These include (1) shallow crustal reverse-faulting events, (2) subduction-interface events, (3) strike-slip events, and (4) normal-faulting events. We exclude a few events with hypocenters deeper than 30 km that are not located at the subduction interface. These include the 2005 $M_w \sim 7.2$ Honshu, Japan, earthquake; the 2006 Pingtung, Taiwan, (doublet, $M_w \sim 6.9$ and ~6.8) earthquakes (Yen *et al.*, 2008); the 2009 $M_w \sim 7.6$ Padang, Indonesia, earthquake; the 2011 $M_w \sim 7.4$ Kermadec Islands, New Zealand, earthquake; and the 2012 $M_w \sim 7.6$ Samar, Philippines, earthquake. Additionally, we remove three single-fault-segment models but retain one model with multiple fault segments for the 2012 $M_w \sim 8.6$ Sumatra earthquake, in view of the rupture complexity of this strike-slip event. In total, our analysis uses 250 rupture models of 130 earthquakes, which include (1) 15 shallow crustal reverse-faulting events with 35 models, (2) 49 subduction-interface events with 101 models, (3) 40 strike-slip events with 75 models, and (4) 23 normal-faulting events with 29 models (Ⓔ Table S1, available in the electronic supplement to this article).

Data Processing

Because earthquake-source inversions *a priori* define the fault plane to estimate the kinematic rupture process, they may overestimate the size of the rupture plane, leading to regions of low (or zero) slips at the fault edges (Somerville *et al.*, 1999; Mai and Beroza, 2000). Some inversion procedures include an iterative reduction of the fault plane to an optimal size or use waveform data to constrain the rupture extents (e.g., Henry *et al.*, 2000). Different approaches and data (e.g., aftershocks catalog) to estimate the initial fault-plane size result in intraevent variability of the rupture dimensions. Hence, the originally defined rupture size could be adequate, overestimated, or even underestimated.

Therefore, it is necessary to implement a consistent measure of rupture dimensions based on the slip distributions. Somerville *et al.* (1999) trimmed slip models by removing rows (and columns) if their average slip is less than 0.3 times the overall average slip. Mai and Beroza (2000) introduced the concept of effective source dimensions, based on the autocorrelation width of the spatially variable slip. Thingbaijam and Mai (2016) extended this approach by applying constraints due to subfault size (spatial grid spacing), locations of large-slip asperities ($u \geq \frac{1}{3} u_{\max}$, Mai *et al.*, 2005), and, if present, surface ruptures.

In this study, we trim each rupture model to its effective source dimension following Thingbaijam and Mai (2016). Slip distributions are expected to taper (to zero or low slip values) at their rupture terminations, due to regions of increased frictional strength (Scholz, 2002; Manighetti *et al.*, 2005). In this context, the autocorrelation width captures the spatial extent of the slip distribution that is consistent with slip tapering and hence the dynamic rupture process. However, we do note that there are exceptions to moderate-to-low absolute slip at the rupture edges. These exceptions include surface rupturing and rupture edges at fault intersections. Therefore, the locations of slip asperities and evidence of surface ruptures are crucial in deciding the effective rupture size.

Regression Analysis

We investigate earthquake source-scaling laws that correlate parameters of rupture geometry, such as rupture width W, length L, area $A(= WL)$, average slip D, and seismic moment M_0. The scaling relationships are generally linear

in double-logarithmic space for the entire range of the data or only parts of it, in the form

$$\log_{10}(y) = b\log_{10}(x) + a. \tag{2}$$

This functional form is simple and well established. In case of moment magnitude M_w (which we adopt in the present study), the functional form is log–linear, which is easily understood from the relationship between M_w and M_0,

$$\log_{10}(M_0) = 1.5M_w + 9.05 \tag{3}$$

(Hanks and Kanamori, 1979), in which M_0 is in newton meters. To develop empirical laws, the slope and intercept (b and a in equation 2) are estimated by regression on the data.

Most studies adopt ordinary least-squares (OLS) regression to derive the scaling relationships (e.g., Wells and Coppersmith, 1994; Leonard, 2010; Strasser *et al.*, 2010). OLS assumes negligible uncertainty of the independent variable compared to the dependent variable. Later, we show that this assumption does not hold. To account for possible measurement errors, Blaser *et al.* (2010) and Rodríguez-Pérez and Ottemöller (2013) applied orthogonal regression (OR). Previously, Stock and Smith (2000) used a generalized version of the OR method. Thingbaijam and Mai (2016) also employed the OR technique to relate magnitude and rupture area. In the present study, we use the GOR technique to derive the relationships to fully consider measurement errors in the analysis.

GOR (Fuller, 1987; Carroll and Ruppert, 1996; Castellaro *et al.*, 2006) minimizes the weighted orthogonal distances of the data points to the regression line, instead of only the vertical distances, and yields a relationship that is interchangeable, such that $y = f(x)$ and $x = f(y)$. It assumes that the variables are linearly related (i.e., applicability of the linear model) and that errors of the variables are independent and normally distributed. The slope b in the linear relation (equation 2) is then computed as follows:

$$b = \frac{\sigma_y^2 - \eta\sigma_x^2 + \sqrt{(\sigma_y^2 - \eta\sigma_x^2)^2 + 4\eta\sigma_{xy}^2}}{2\sigma_{xy}}, \tag{4}$$

in which σ_x^2, σ_y^2, and σ_{xy} denote the sample variance of x, variance of y, and covariance between x and y, respectively. When the error-variance ratio of the variables, $\eta(= \sigma_y^2/\sigma_x^2)$, is equal to 1, equation (4) corresponds to OR. Based on the estimated slope, the intercept is calculated as

$$a = \bar{y} - b\bar{x}, \tag{5}$$

in which $\bar{x}$ and $\bar{y}$ are the average values of x and y.

Currently, the available data on earthquake source parameters, specifically for multiple intraevent rupture models, are not sufficient for reliable (empirical) analysis of measurement errors. Therefore, we take a different perspective on this problem with respect to previous studies when evaluating source parameters independently, for instance, earthquake magnitude, surface-rupture length, and surface displacement (Bonilla *et al.*, 1984; Wells and Coppersmith, 1994) by relating this problem to the computation of seismic moment. Following Aki (1966), the fundamental equation is given by

$$M_0 = \mu AD, \tag{6}$$

in which μ is crustal rigidity (usually assumed constant, and typically $\mu = 3.3 \times 10^{10}$ N·m^{-2}). It implies that the error variances of A and D control that of M_w (see also equation 3). We can therefore express the error variance of moment magnitude in terms of the error variances of $\log_{10} A$ and $\log_{10} D$ (denoted by $\sigma^2_{\log_{10} A}$ and $\sigma^2_{\log_{10} D}$) as

$$\sigma^2_{M_w} = \frac{4}{9}(\sigma^2_{\log_{10} A} + \sigma^2_{\log_{10} D}). \tag{7}$$

Similarly, the error variance of $\log_{10} A$ can be expressed as

$$\sigma^2_{\log_{10} A} = \sigma^2_{\log_{10} L} + \sigma^2_{\log_{10} W}. \tag{8}$$

We hypothesize that the measurement errors of L, W, and D are independent and identically distributed random variables, affected by the above-described parameterization and modeling assumptions that govern source-inversion uncertainties. We note that published empirical relationships predicting $\log_{10} A$ and $\log_{10} D$ from M_w have comparable standard errors (e.g., Mai and Beroza, 2000; Goda *et al.*, 2016), similarly for relationships that predict $\log_{10} L$ and $\log_{10} W$ from M_w. Therefore, we assume that the error variances of $\log_{10} A$ and $\log_{10} D$ are comparable.

To realize the first-order estimates of the error-variance ratio, we consider that error variances of $\log_{10} L$ and $\log_{10} W$ are of the same order. Such an assumption is usually adopted if parameters with unknown measurement errors have been computed by the same method. We note that source inversions of geodetic data or near-source waveforms are associated with the limited resolution of slip at depth (e.g., Zhou *et al.*, 2004; Page *et al.*, 2009) that may lead to a larger uncertainty of W (compared to that of L). However, our database includes a larger number of source models from teleseismic and joint inversions, as well as multiple source models for many events, justifying our assumption. Thus, combining equations (7) and (8), we obtain

$$\frac{\sigma^2_{\log_{10} L}}{\sigma^2_{M_w}} \sim \frac{\sigma^2_{\log_{10} W}}{\sigma^2_{M_w}} \sim \frac{9}{16}. \tag{9}$$

Consequently, the measurement error of M_w is larger than, and independent of, those of L, W, and D, if these physical parameters are individually considered.

The actual datasets are likely to have an error-variance ratio somewhat different from these estimates, due to factors such as data sampling, inherent data scatter (aleatoric), and

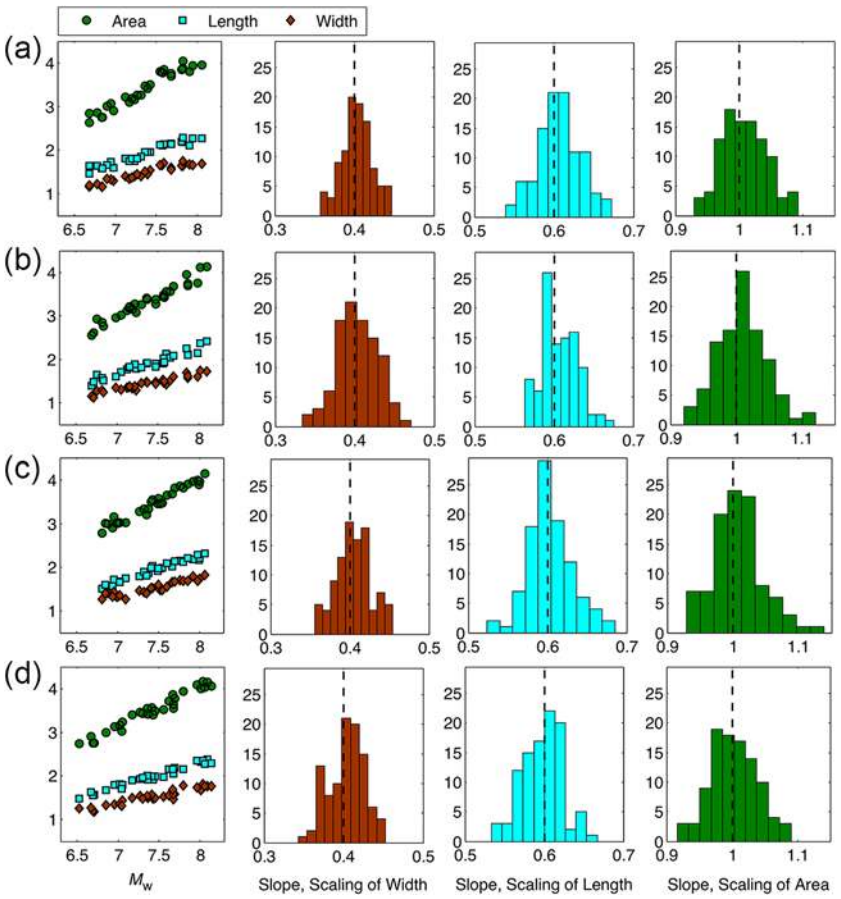

Figure 3. Generalized orthogonal regressions (GORs) carried out with randomly generated 100 synthetic datasets of magnitude M_w and $\log_{10} Y$, in which Y is either width W (km), length L (km), or area A (km^2), such that the error-variance ratios are fixed with applied standard deviations for M_w, W, and L equal to (a) 0.100, 0.075, and 0.075, (b) 0.100, 0.030, and 0.030, (c) 0.100, 0.030, and 0.095, and (d) 0.100, 0.095, and 0.095. The leftmost column depicts crossplots between magnitude M_w and $\log_{10} Y$ from a single dataset. The histograms show the distributions of the mean slope estimated with $\eta = 0.5625$, using the realizations of datasets. The dashed line on each histogram indicates the true slope parameter. The color version of this figure is available only in the electronic edition.

heteroscedasticity (variable η for different data points). Furthermore, GOR analyses may yield scaling relationships that do not exactly correlate the scaling of L and W with that of A. Such inconsistency would be marginal but can be avoided by computing the scaling relationship of A from those of W and L, instead of direct regression (e.g., Blaser *et al.*, 2010). Given these factors, it is necessary to confirm whether the first-order theoretical estimates of the error-variance ratio are appropriately chosen.

To do so, we use synthetic tests. We generate test datasets considering slopes equal to 0.4 and 0.6 for $M_w - \log_{10} W$ and $M_w - \log_{10} L$ for uniformly distributed M_w values. The choice of these slope values is motivated considering previously published scaling relations (e.g., Mai and Beroza, 2000; Leonard, 2010). Then, we apply normally distributed random errors adjusted to achieve the desired error-variance ratio.

As depicted in Figure 3, we consider four cases: (1) error variances according to the theoretical estimates (equation 9), (2) a smaller error for both $\log_{10} W$ and $\log_{10} L$ compared to the theoretical estimates ($\sigma^2_{\log_{10} W}/\sigma^2_{M_w} = 0.09$ and $\sigma^2_{\log_{10} L}/\sigma^2_{M_w} = 0.09$), (3) a larger error for $\log_{10} W$ and a smaller one with $\log_{10} L$ than the theoretical estimates ($\sigma^2_{\log_{10} W}/\sigma^2_{M_w} = 0.90$ and $\sigma^2_{\log_{10} L}/\sigma^2_{M_w} = 0.09$), and (4) a larger error for both $\log_{10} W$ and $\log_{10} L$ compared to the theoretical estimates ($\sigma^2_{\log_{10} W}/\sigma^2_{M_w} = 0.90$ and $\sigma^2_{\log_{10} L}/\sigma^2_{M_w} = 0.90$). The error variance of M_w is fixed in all these cases. Because the data are limited in practice, we generate only 30 pairs of data points each time and apply GOR using the theoretical estimates of η. Figure 3 shows that the distributions of the estimated slope b have comparable scatter in all four cases. Overall, the distributions exhibit marginal shifts of the peak (highest probability) from the actual values, although these shifts do not statistically impact the scaling behavior implied by the slope b. Thus, we conclude that the theoretical estimates of η are practical and adequate for the regression analysis.

To analyze the present dataset, we first develop the scaling relationships between M_w and $\log_{10} W$ and between M_w and $\log_{10} L$. Then, we apply these relationships using the definition of seismic moment (equations 3 and 6) in the regressions to develop the remaining scaling laws. This approach is similar to Leonard (2010); however, we avoid prior assumptions on the scaling coefficients and also on fault-aspect ratio (L/W). During the regression, we estimate the errors (standard deviations) for the scaling coefficients using the delete-one jackknife technique (Efron, 1982).

We also validate the developed linear models by testing for the normality of the residuals, using the Lilliefors test (Lilliefors, 1967) and the Shapiro–Wilk test (Shapiro and Wilk, 1965). The Lilliefors test evaluates the statistical significance based on the maximum discrepancy between the empirical cumulative distribution and the normal cumulative distribution to reject the null hypothesis (i.e., the normally distributed data). The Shapiro–Wilk test applies a frequency measure based on normal scores (Ghasemi and Zahediasl, 2012). In both tests, we consider a significance level of 0.05. The null hypothesis is rejected if the test statistics result in $h = 1$, otherwise, it is not rejected. On the other hand, if p (or p-value) is larger than the significance level, the null hypothesis is not rejected.

Table 1
Scaling Coefficients between Rupture Length, Rupture Width, Rupture Area, and Moment Magnitude

Faulting Regime	Equation	b (sb)	a (sa)	σ	r^2	Data Range	
						M_w	Dimension
Reverse faulting (shallow crustal)	$\log_{10} L = a + bM_w$	0.614 (0.043)	−2.693 (0.292)	0.083	0.93	5.59–7.69	4.9–108.0 km
	$\log_{10} W = a + bM_w$	0.435 (0.050)	−1.669 (0.336)	0.087	0.90	5.59–7.69	4.8–45.0 km
	$\log_{10} A = a + bM_w$	1.049 (0.066)	−4.362 (0.445)	0.121	0.94	5.59–7.69	23.5–4, 860.0 km^2
Subduction interface	$\log_{10} L = a + bM_w$	0.583 (0.037)	−2.412 (0.288)	0.107	0.85	6.68–9.19	29.2–1420.0 km
	$\log_{10} W = a + bM_w$	0.366 (0.031)	−0.880 (0.243)	0.099	0.75	6.68–9.19	29.2–260.0 km
	$\log_{10} A = a + bM_w$	0.949 (0.049)	−3.292 (0.377)	0.150	0.86	6.68–9.19	852.6–318, 080.0 km^2
Normal faulting	$\log_{10} L = a + bM_w$	0.485 (0.036)	−1.722 (0.260)	0.128	0.88	5.86–8.39	9.0–262.5 km
	$\log_{10} W = a + bM_w$	0.323 (0.047)	−0.829 (0.333)	0.128	0.77	5.86–8.39	6.0–112.5 km
	$\log_{10} A = a + bM_w$	0.808 (0.059)	−2.551 (0.423)	0.181	0.88	5.86–8.39	54.0–29, 531.3 km^2
Strike slip	$\log_{10} L = a + bM_w$	0.681 (0.052)	−2.943 (0.357)	0.151	0.88	5.38–8.70	6.0–580.0 km
	$\log_{10} W = a + bM_w$	0.261 (0.026)	−0.543 (0.179)	0.105	0.75	5.38–8.70	6.5–50.0 km
	$\log_{10} A = a + bM_w$	0.942 (0.058)	−3.486 (0.399)	0.184	0.88	5.38–8.70	39.0–29, 000.0 km^2

Scaling coefficients were obtained by general orthogonal regressions, except for the scaling relationships between moment magnitude and rupture area, which were calculated using those of rupture length and rupture width. The notations in the equations: L, W, A, and M_w denote rupture length, rupture width, rupture area, and moment magnitude. The slope and intercept are given by a and b, their standard errors by sa and sb, while the standard deviation is given by σ. The correlation coefficient is denoted by r^2.

Empirical Scaling Laws for Rupture Dimensions

To put our new empirical scaling laws in context, let us first discuss a few widely accepted concepts of earthquake source-scaling. An often-cited scaling behavior is that of self-similarity, which implies that any change in M_0 requires proportional changes in W, L, and D (Kanamori and Anderson, 1975). Accordingly, the relations between fault parameters and seismic moment (moment magnitude) take on the form $L \propto M_0^{1/3}$, $W \propto M_0^{1/3}$, $D \propto M_0^{1/3}$, and $A \propto M_0^{2/3}$. This scaling behavior assumes a constant fault-aspect ratio (L/W) and is associated with scale-invariant stress drop.

Regardless of whether or not stress drop is scale-invariant, the $A \propto M_0^{2/3}$ scaling has been observed to be consistent with empirical scaling relationships (Wells and Coppersmith, 1994; Somerville *et al.*, 1999; Hanks and Bakun, 2002; Murotani *et al.*, 2008; Leonard, 2010; Skarlatoudis *et al.*, 2016). On the other hand, several studies reported that L grows faster with increasing magnitude ($M_w > 6$) compared to the growth of W (e.g., Mai and Beroza, 2000; Henry and Das, 2001; Papazachos *et al.*, 2004; Blaser *et al.*, 2010; Leonard, 2010).

For very large strike-slip earthquakes occurring on quasivertical faults, the seismogenic depth restricts the growth of W. Depending on whether D is controlled by L or W, the two different paradigms of the L model and the W model have been debated. The L model proposes that D scales with L. In contrast, in the W model, D is independent of L (Scholz, 1982, 1994). The L model exhibits $M_0 \propto L^2$ scaling and is supported by empirical evidences (e.g., Pegler and Das, 1996). On the other hand, the W model agrees with dislocation theory and shows $M_0 \propto L$ scaling, once W is bounded by the finite seismogenic depth of the crust (Romanowicz, 1992; Romanowicz and Ruff, 2002). It also has been suggested that the average slip could be between these two end-member models (Bodin and Brune, 1996; Blaser *et al.*, 2010; Leonard, 2010). King and Wesnousky (2007) proposed that constant stress-drop scaling for strike-slip earthquakes could be realized if coseismic slip occurs below the seismogenic zone. Recent physical and theoretical models explored this hypothesis (e.g., Shaw and Wesnousky, 2008; Shaw, 2009; Jiang and Lapusta, 2016).

In the present study, we do not apply any theoretical constraints *a priori* on the regression analysis, but we relate to them when discussing the empirical scaling laws. In the following subsections, we describe the empirical scaling laws for W, L, and A for the different faulting regimes. Table 1 lists the scaling coefficients between M_w and $\log_{10} W$, $\log_{10} L$, and $\log_{10} A$ given by the regressions. We also compare our results with independent datasets of previous studies. Additionally, we examine the scaling properties of fault-segment dimensions for multisegment rupture models.

Magnitude versus Rupture Width

Strike-slip events on quasivertical faults are strongly affected by the finite width of the seismogenic layer. However, the thickness of the seismogenic layer varies from continental to oceanic crust, across back-arc and fore-arc regions along subduction zones, and even along major strike-slip faults traversing different geological-tectonic units. We first investigate the linear and bilinear relationships of M_w versus $\log_{10} L$, considering only continental strike-slip events and taking into account the scaling of W (see the Appendix). We note that the scatter in the data does not allow for a clear discrimination between linear and bilinear relationships for M_w versus $\log_{10} L$ (Figs. A1 and A2). However, we find that W grows gradually with increasing M_w and does not saturate as expected from the W model. This finding supports a linear relationship, rather than a bilinear one. Therefore, we apply linear relationships to evaluate the source-scaling properties of strike-slip earthquakes.

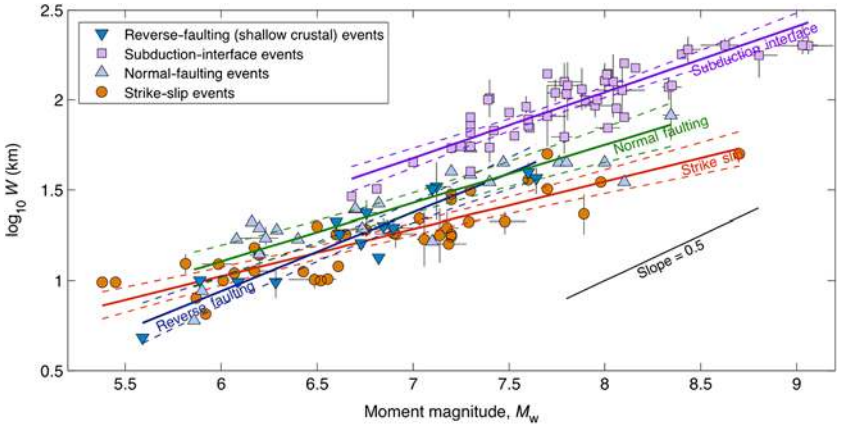

Figure 4. The regressions between moment magnitude M_w and rupture width W; solid and dashed lines correspond to the linear fits given by GORs and the 95% confidence intervals, respectively. If multiple-rupture models for the same event exist, the data point corresponds to the mean of the logarithm-transformed data, whereas the bars indicate the corresponding ranges. The scaling coefficients are listed in Table 1. The growth of W with increasing M_w is different for the different faulting regimes. We also observe that W for strike-slip events does not saturate but grows very slowly with M_w. Detailed plots for each faulting regime and the analysis of the residuals can be found in Ⓔ Figures S1 and S2 (available in the electronic supplement to this article). The color version of this figure is available only in the electronic edition.

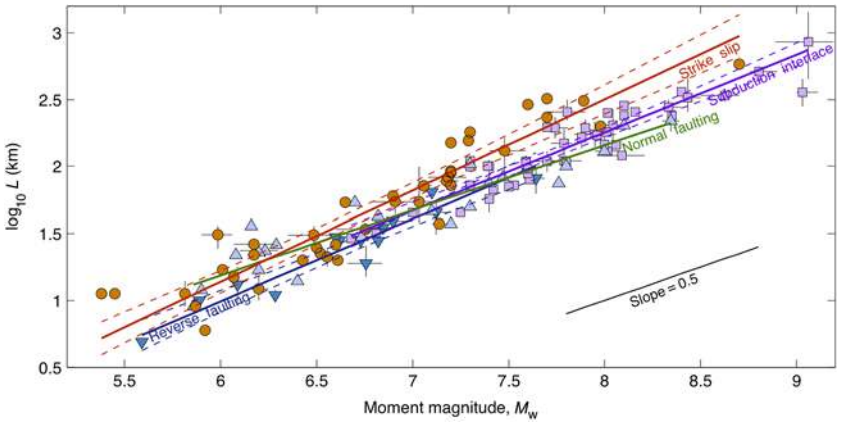

Figure 5. Same as Figure 4 but for the regressions between moment magnitude M_w and rupture length L. We find that L grows much faster for strike-slip events with increasing M_w compared to other faulting regimes. The scaling coefficients are listed in Table 1. Detailed plots for each faulting regime and the analysis of the residuals can be found in Ⓔ Figures S3 and S4. The color version of this figure is available only in the electronic edition.

Figure 4 plots the regression analyses of $\log_{10} W$ against M_w for the different faulting regimes (Ⓔ see Fig. S1 for separate plots for each faulting regime). Statistical tests do not reject normally distributed residuals (Ⓔ Fig. S2). We observe that there are systematic deviations from self-similar scaling in the growth of W with increasing M_w among the different faulting regimes, with slow-to-rapid W increase from strike-slip, normal-faulting, subduction-interface, and crustal reverse-faulting events. In fact, the relationship for shallow crustal reverse-faulting events is close to self-similar scaling (with slope ~0.44).

Compared to other faulting regimes, subduction-interface events are associated with much larger W for a given M_w. Normal-faulting and strike-slip earthquakes (in this order) have larger W than crustal reverse-faulting earthquakes for lower magnitudes but smaller W for larger magnitudes. This transition of regimes comes at $M_w \sim 6.5$ and ~7.4 for strike-slip and normal-slip events, respectively, relating to the differences in the slope of the scaling relationships: 0.44 (reverse faulting), 0.32 (normal faulting), and 0.26 (strike slip).

An important question is whether rupture models for megathrust events ($M_w > 8.5$) saturate in W (owing to finite down-dip seismogenic depth). Several lines of arguments can be made to address this issue. First, we have very few events (only four) in this magnitude range, although a median estimate of $W \sim 200$ km is consistent. Similar median values across a narrow range of magnitude are not unusual, considering the inherent uncertainties of W estimates. Second, compared to the global distribution of average seismogenic depth (Herrendörfer *et al.*, 2015), these estimates of W are within the bounds of the down-dip seismogenic depth, except for the 2011 Tohoku earthquake. In addition, the fault-dip and down-dip seismogenic depths vary across different seismotectonic regions (Pacheco *et al.*, 1993; Llenos and McGuire, 2007). Third, earthquake ruptures have been observed to extend down-dip into the aseismic regions. Hence, W may not be constrained by the seismogenic depth only (e.g., Kanamori and McNally, 1982; Strasser *et al.*, 2010; Jiang and Lapusta, 2016). Based on these factors, we conclude that a width saturation of megathrust earthquakes is currently not evident, specifically at the global scale, although it may occur in specific subduction zones (even at segments of a subduction zone). Previously, Skarlatoudis *et al.* (2016) arrived at a similar conclusion.

Magnitude versus Rupture Length

Figure 5 depicts the regression analysis between M_w and $\log_{10} L$ for different faulting regimes. In Ⓔ Figure S3, we provide separate plots for each faulting regime. Statistical tests support normally distributed residuals (Ⓔ Fig. S4). The linear relationships for crustal reverse-faulting events and subduction-interface events have similar slopes ($b \sim 0.6$) that are inconsistent with self-similar scaling.

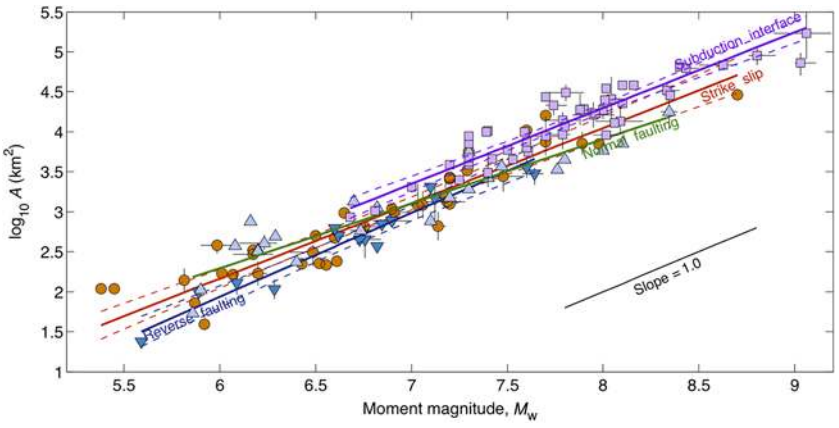

Figure 6. Same as Figure 4 but for the regressions between moment magnitude M_w and rupture area A. Except for normal-faulting events, the scaling behavior is statistically consistent with self-similar scaling. Subduction-interface events have the largest rupture area for a given magnitude. At the lower magnitude range ($M_w < 6.5$), reverse-faulting (shallow crustal) events have the smallest rupture area for a given magnitude. The scaling coefficients are listed in Table 1. Detailed plots for each faulting regime and the analysis of the residuals can be found in Ⓔ Figures S5 and S6. The color version of this figure is available only in the electronic edition.

Our scaling relationship for subduction-interface events is more consistent with the very long rupture (~1000 km) associated with the 2004 $M_w \sim 9.1$ Sumatra earthquake, compared to the effective rupture length (~350 km) associated with the 2011 $M_w \sim 9.0$ Tohoku earthquake (although the regression analysis includes them both). However, the Tohoku earthquake has been associated with exceptionally complicated rupture processes, with possible repeated rupturing of asperities (e.g., Lee *et al.*, 2011; Galvez *et al.*, 2016).

Interestingly, the scaling of L for normal-faulting events supports self-similar scaling. This observation is statistically consistent, even when excluding outer-rise and in-slab events. Our analysis leads us to speculate that self-similar scaling occurs at smaller magnitudes ($M_w < 5.5$) for strike-slip, normal-faulting, and reverse-faulting earthquakes. Such convergence to self-similar scaling could occur at $M_w < 7.0$ for the subduction-interface earthquakes.

With slope ~0.7 in the scaling relationship (close to that implied by the L model), we find that length L of strike-slip events grows much faster with M_w, compared to other faulting regimes (Fig. 5). The scaling relationship developed using all strikes-slip events does not show statistically significant differences from that obtained using only the continental events (Figs. A1 and A2). Additionally, the 2012 $M_w \sim 8.7$ Sumatra earthquake had a very complex rupture mechanism that consisted of multiple individual ruptures (Yue *et al.*, 2012). However, exclusion of this outlier event does not significantly impact the regressions.

Magnitude versus Rupture Area

Although the scaling of W and L with respect to M_w often deviates from self-similar scaling, the scaling of A is overall statistically consistent with self-similarity, except for normal-faulting earthquakes (Fig. 6 and Ⓔ Figs. S5 and S6). Generally, the growth of W with increasing M_w is slower than predicted by self-similar scaling, which, however, is compensated for by a more-rapid growth of L with increasing M_w, leading in combination to self-similar scaling. However, this is not the case for normal-faulting events, which show self-similar scaling of L but not of W.

For a given magnitude, subduction-interface earthquakes generally occupy the largest rupture area, whereas shallow crustal reverse-faulting earthquakes are the smallest. The scaling relationships also predict that strike-slip and normal-faulting events with larger magnitudes ($M_w > 7.5$) occupy a rupture area that is comparable (or smaller) than that of shallow crustal reverse-faulting events.

Scaling of Average Slip

Let us examine how D relates with W, L, A, and M_w. The scaling coefficients obtained from the GOR analysis are given in Table 2. The correlations (indicated by the correlation coefficient) are poor between $\log_{10} W$ and $\log_{10} D$, except for shallow crustal reverse-faulting events, but are somewhat higher between $\log_{10} L$ and $\log_{10} D$ (Ⓔ see Figs. S7 and S8). As shown in Figure 7, the relationships between $\log_{10} A$ and $\log_{10} D$ generally agree with self-similar scaling of A and are consistent with the definition of M_0, such that $D \propto A^{0.5}$. However, normal-faulting events tend to deviate from self-similar scaling. Thus, for a specific faulting regime, the scaling of D with A can be identified with how A scales with M_w.

Likewise, the regressions between M_w and $\log_{10} D$ are statistically consistent with self-similar scaling with slope $b \sim 0.5$, except for the normal-faulting events (Ⓔ see Fig. S9). We note that the average slip associated with the 2011 Tohoku earthquake was exceptionally large. In general, the scatter associated with the scaling of D (either with respect to A or M_w) suggests possible variability of stress drop within each faulting regime.

Comparisons with Independent Dataset and Previous Studies

To evaluate our new empirical scaling laws against independent data, we use the compilation by Blaser *et al.* (2010) whose original data sources are Wells and Coppersmith (1994), Geller (1976), Scholz (1982), Mai and Beroza (2000), Konstantinou *et al.* (2005), and several other authors. To completely decouple it from the present database, we exclude the data used by Mai and Beroza (2000). We also

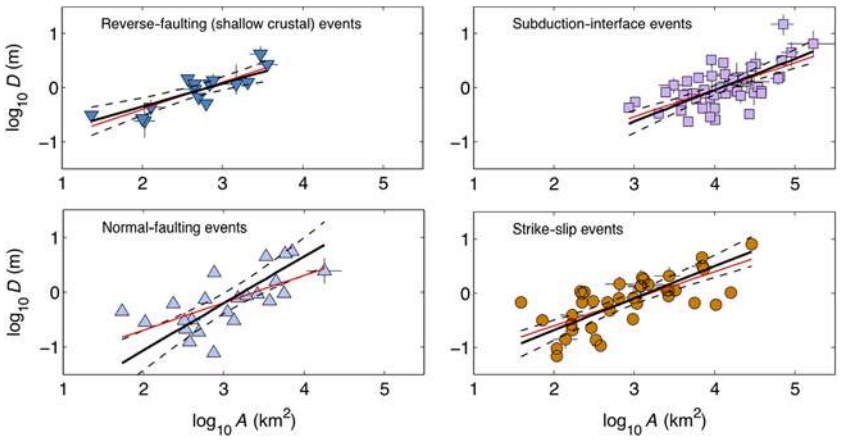

Figure 7. Regressions between rupture area A and average displacement D (in solid black lines, with the 95% confidence intervals shown by dashed lines) are more or less statistically consistent with self-similar scaling of $A \propto D^{0.5}$ (shown by the lighter lines), except for normal-faulting events, which tends to deviate from this scaling behavior. The scaling coefficients are listed in Table 2. The color version of this figure is available only in the electronic edition.

exclude the data for events prior to 1964, for which we consider the source-parameter estimates to be much-less accurate (e.g., Blaser *et al.*, 2010). Instead of conducting additional regressions with this alternative dataset, we calculate residuals (difference between actual and predicted value) by applying our empirical scaling relationships to this dataset.

Figure 8 shows the distributions of residuals with respect to magnitude. For M_w versus $\log_{10} L$, the scaling relationships agree reasonably well with the dataset (indicated by the mean trend close to 0), except for subduction-interface events with mostly negative residuals (Fig. 8a). In the case of M_w versus $\log_{10} W$, our scaling laws generally predict larger W. The residuals are negatively biased for strike-slip earthquakes and strongly so for subduction-interface and normal-faulting events (Fig. 8b).

Our analysis of residuals suggests that aftershock maps generally produce smaller W compared to the source inversions. This difference is remarkable for subduction-interface and normal-faulting events, especially for those located in the oceanic crust. Taking into account the aspects of data quality and inherent statistical scatter, we conclude that our new empirical scaling laws are compatible with the independent dataset of Blaser *et al.* (2010).

For reverse-faulting shallow crustal events, the present study generally agrees with the previous ones in predicting W, L, and A from magnitude (Ⓔ Table S2 and Fig. S10). However, we do not corroborate the scaling coefficients for W (specifically, slope) given by Wells and Coppersmith (1994) and Leonard (2010). Furthermore, the new scaling laws predict shorter L compared to these studies, including Blaser *et al.* (2010), but longer L for a given magnitude compared to Mai and Beroza (2000). Nevertheless, the scaling of A is consistent with self-similar scaling (Somerville *et al.*, 1999; Thingbaijam and Mai, 2016).

Likewise, for subduction-interface events, the comparison with previous studies reveals an interesting pattern, with more-recent studies revealing longer W and L (Ⓔ Table S3 and Fig. S11). In this respect, our new scaling relationships are close to those given by Goda *et al.* (2016) and Skarla-

Table 2
Scaling Coefficients between Average Slip, Rupture Width, Rupture Length, Rupture Area, and Moment Magnitude

Faulting Regime	Equation	b (sb)	a (sa)	σ	r^2
Reverse faulting (shallow crustal)	$\log_{10} D = a + bM_w$	0.451 (0.093)	−3.156 (0.639)	0.149	0.77
	$\log_{10} D = a + b\log_{10} A$	0.429 (0.134)	−1.213 (0.379)	0.180	0.72
	$\log_{10} D = a + b\log_{10} L$	0.975 (0.203)	−1.456 (0.309)	0.132	0.78
	$\log_{10} D = a + b\log_{10} W$	0.767 (0.397)	−1.022 (0.522)	0.200	0.58
Subduction interface	$\log_{10} D = a + bM_w$	0.552 (0.067)	−4.226 (0.526)	0.171	0.74
	$\log_{10} D = a + b\log_{10} A$	0.582 (0.136)	−2.375 (0.558)	0.257	0.35
	$\log_{10} D = a + b\log_{10} L$	1.092 (0.223)	−2.320 (0.477)	0.213	0.34
	$\log_{10} D = a + b\log_{10} W$	1.244 (0.577)	−2.438 (1.154)	0.213	0.25
Normal faulting	$\log_{10} D = a + bM_w$	0.693 (0.066)	−4.967 (0.484)	0.195	0.86
	$\log_{10} D = a + b\log_{10} A$	0.858 (0.214)	−2.779 (0.683)	0.330	0.29
	$\log_{10} D = a + b\log_{10} L$	1.302 (0.303)	−2.302 (0.531)	0.252	0.43
	$\log_{10} D = a + b\log_{10} W$	2.512 (0.842)	−3.698 (1.216)	0.223	0.00
Strike slip	$\log_{10} D = a + bM_w$	0.558 (0.054)	−4.032 (0.376)	0.227	0.77
	$\log_{10} D = a + b\log_{10} A$	0.593 (0.112)	−1.875 (0.342)	0.302	0.43
	$\log_{10} D = a + b\log_{10} L$	0.789 (0.144)	−1.473 (0.259)	0.276	0.48
	$\log_{10} D = a + b\log_{10} W$	2.391 (0.485)	−3.092 (0.602)	0.178	0.10

Scaling coefficients were obtained by general orthogonal regressions. The notations are as in Table 1. D, A, and M_w denote average slip (in m), rupture area (in km^2), and moment magnitude.

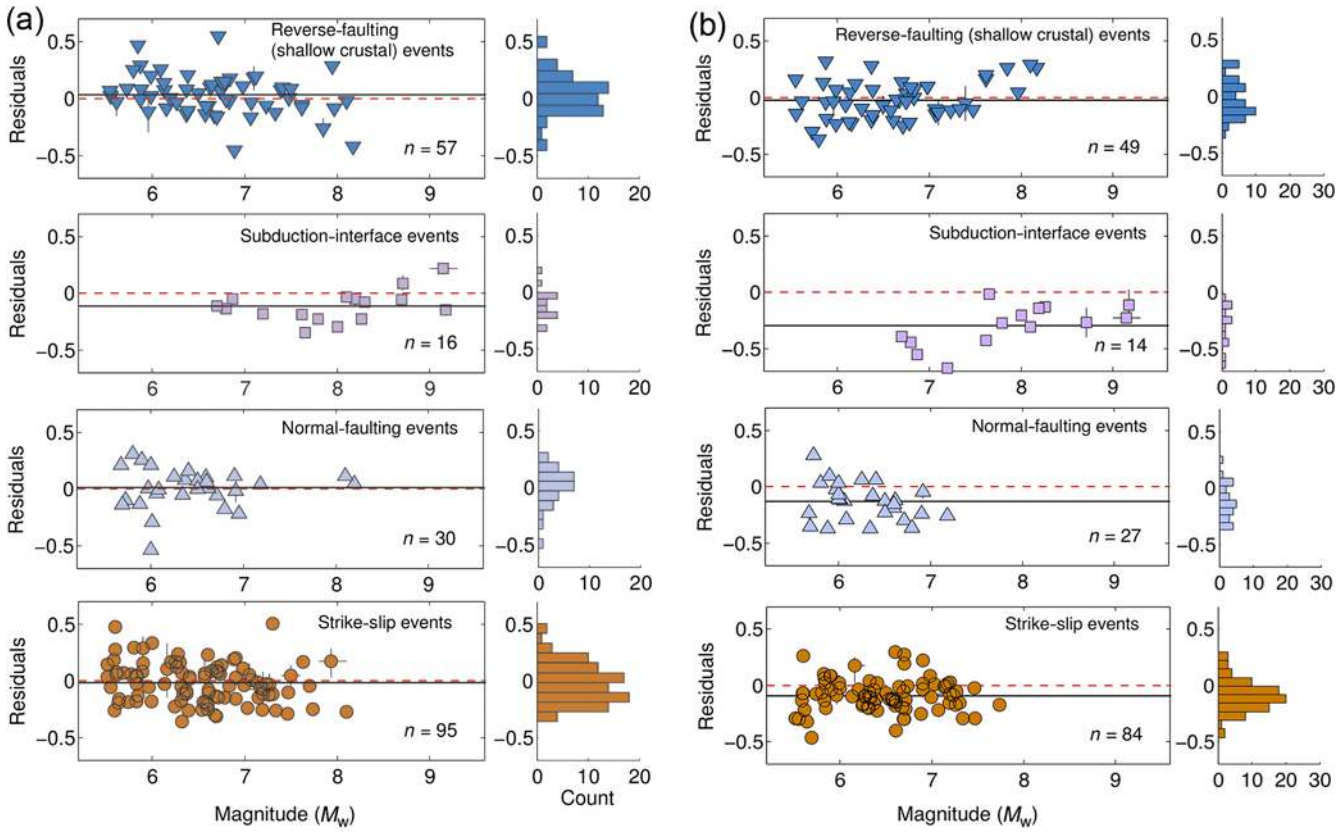

Figure 8. Histograms and distributions of the residuals (difference between actual and predicted value on $\log_{10}$ scale) with respect to moment magnitude M_w: (a) for rupture length and (b) for rupture width, classified according to the different faulting regimes. The actual values correspond to the dataset of Blaser *et al.* (2010), and predicted values are obtained by applying our new empirical scaling relationships. Note the general agreement between the mean residual (solid line) and the zero-mean trend (dashed line), except for the scaling of rupture width for subduction-interface, strike-slip, and normal-faulting events. The color version of this figure is available only in the electronic edition.

toudis *et al.* (2016). However, our scaling relationship between M_w and $\log_{10} W$ for subduction-interface events overall differs from the previous studies. The scaling of L compares well with Leonard (2010) but predicts longer L compared to Strasser *et al.* (2010) and Blaser *et al.* (2010). Considering scaling relationships of A and W with respect to M_w developed by Skarlatoudis *et al.* (2016), we find that their scaling relationship for L approximates the L model ($M_w - \log_{10} L$ scaling with slope ~0.7) different than this study. The present study also corroborates self-similar scaling of A for the subduction-interface events (e.g., Murotani *et al.*, 2013; Skarlatoudis *et al.*, 2016; Thingbaijam and Mai, 2016).

For normal-faulting events, the new scaling coefficients suggest longer W, and consequently larger A, compared to previous studies (Ⓔ Table S4 and Fig. S12). As the scaling relationship given by Blaser *et al.* (2010) predicts longer L for a given magnitude, we find that it predicts A similar to the new relationship, especially at larger magnitudes ($M_w > 6.5$). We note that the scaling relationships between M_w and A deviate from the self-similar one and can be attributed to slower growth of W with increasing M_w.

Regarding strike-slip events, the new empirical scaling laws predict larger W than previous studies for a given magnitude (Ⓔ Table S5 and Fig. S13). However, there is a general agreement in the prediction of L with Wells and Coppersmith (1994) and Blaser *et al.* (2010). The empirical scaling law for L is inclined toward the L model, and hence differs from Mai and Beroza (2000) and Leonard (2010). Our relations also differ from those of Hanks and Bakun (2002, 2008), although the authors adopted the L-model scaling, because we find that the scaling of A is not strongly affected by the finite seismogenic depth. In our finding, the growth of L is more rapid but that of W is restricted (but not saturated) with the increasing M_w.

The differences between our current study and the work of Mai and Beroza (2000) can be explained by considering the computation of effective source dimensions. Mai and Beroza (2000) computed the effective source dimensions based on the autocorrelation widths of the along-strike- and down-dip-averaged slip distribution. Here, we apply adjustments to the autocorrelation width following Thingbaijam and Mai (2016), which provide larger source dimensions. Additionally, the data used in the present study significantly

differ from Mai and Beroza (2000) in terms of magnitude coverage and number of events.

To further compare with previous studies, not only the use of different datasets needs to be accounted for but also the regression techniques used (including possible constraints on the slope). The different regression techniques treat the errors-with-variables either implicitly or explicitly (as discussed previously); however, whether or not the estimated coefficients agree or differ statistically would depend largely on the data scatter. For instance, Goda *et al.* (2016) obtained scaling coefficients using linear regressions different from the present study based on GOR, although they used almost the same dataset. Hence, these differences are due to the applied regression techniques.

In this context, we make a brief note on the regression techniques. GOR generally provides a larger slope compared to OLS regression, depending on the error-variance ratio between two variables. For significantly smaller measurement errors of x (compared to those of y), the slopes estimated by the two techniques could be comparable. However, in the present analyses, measurement errors of x (i.e., M_w) are larger than those of y (i.e., $\log_{10} W$ or $\log_{10} L$, as explained in the Regression Analysis section). Nevertheless, a key factor in the contrasts between different regression techniques would be wide data scatter. Narrowly scattered data would produce similar regressions, irrespective of the applied techniques.

Similarly, our source-scaling relationships for strike-slip events deviate from that of Blaser *et al.* (2010), possibly due to differences in the regression technique and/or the absence of very large events in their database. They applied OR that assumes a unit error-variance ratio of both variables (e.g., M_w and $\log_{10} L$). However, the definition of M_w implies that the measurement errors of M_w are larger than those for $\log_{10} L$ (or $\log_{10} W$), and hence the error-variance ratio is not unity. Thingbaijam and Mai (2016) also used ORs but for regressions between $\log_{10} M_0$ and $\log_{10} A$. In this regard, the present scaling laws supersede our previous ones. Nevertheless, these differences do not affect the key finding of Thingbaijam and Mai (2016) that earthquake-slip distributions follow a truncated exponential law.

A closer agreement of our scaling relations with the ones given by Strasser *et al.* (2010) could be due to a more-similar dataset, because they include rupture models from a previous version of the SRCMOD database. We also note that Blaser *et al.* (2010) and Leonard (2010) did not differentiate reverse-faulting events from shallow crustal and subduction-interface events but considered them as a single category. We attribute this similarity in source-scaling coefficients (between shallow crustal and subduction-interface events) to their datasets.

Impact of Data Used for Source Inversions

Different kinds of data and methods have been used in finite-fault source inversions to generate the rupture models that eventually form the dataset used in our study. Therefore, we examine how this affects model resolution and consequently the effective source dimensions. Geodetic data (Global Positioning System and Interferometric Synthetic Aperture Radar observations) are known to have limited sensitivity to slip on the deeper parts of the faults (e.g., Page *et al.*, 2009). Similar limitations apply to near-field strong-motion data (e.g., Zhou *et al.*, 2004). Teleseismic recordings allow constraining the overall rupture properties at larger scales but are poor in resolving the temporal details. Strong-motion data help resolve the finer details of the rupture process, but their spatial distribution strongly affects the inversion results. Joint inversion (e.g., the combination of seismic and geodetic data) produces robust rupture models, but often degrades the data fits for the individual datasets. These effects on the rupture models require further evaluation, specifically in terms of possible bias introduced by any of the source-inversion aspects.

Figure 9 displays box plots that depict the distributions of the differences between parameter values ($\log_{10} W$ and $\log_{10} L$) predicted by our empirical scaling laws and those given by a specific rupture model. The rupture models are grouped according to four broad data categories used in source inversions: strong-motion data, teleseismic recordings, geodetic data (including tsunami data), and joint (combination of seismic and geodetic data). Unlike the regression analyses, we perform this assessment on each rupture model, even if multiple source models exist for the same earthquake. Thus, the box plots capture both interevent and intraevent variabilities of the rupture models with respect to the empirical scaling laws. For the empirical scaling laws, we anticipate that the interevent and intraevent variabilities are comparable in predicting the parameters required for seismic-hazard analysis. This conjecture is well attested to by the observed intraevent variability (Figs. 5–7; see also Gomberg *et al.*, 2016) and from the exercises of the source-inversion validation project (Mai *et al.*, 2016).

Figure 9 shows that the variability in estimates of $\log_{10} W$ and $\log_{10} L$, considering the entire range of the distribution (described by the box plots), increases with the number of rupture models and typically does not depend on the data used for the inversions. Furthermore, the distributions between the first and third quartiles (i.e., 50% of the data) generally overlap each other, indicating that statistically the different datasets used in the inversions do not strongly affect the inferred source-scaling properties. However, this observation does not hold for the geodetic inversions (of strike-slip events), which provide smaller W compared to the seismic and joint inversions. Nevertheless, with only six geodetic inversions (out of a total of 75 rupture models) for the strike-slip events, the empirical scaling laws are hardly affected.

Scaling of Oblique-Slip Events

When considering the dominant faulting types for classifying the earthquake mechanism, the presence of

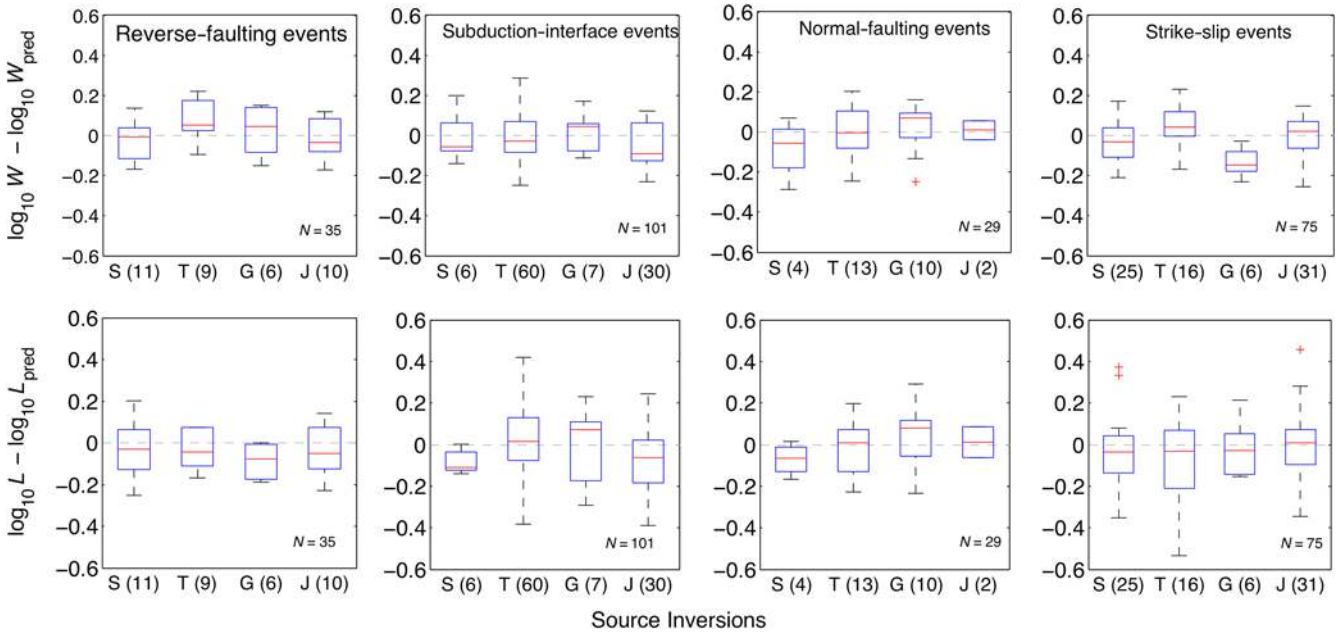

Figure 9. The box plots depict the distributions of the differences between the parameter (rupture width W and rupture length L) predicted by the empirical scaling laws ($\log_{10} W_{pred}$ and $\log_{10} L_{pred}$) and that given by a specific rupture model ($\log_{10} W$ and $\log_{10} L$). We group the rupture models according to the data used for the source inversions: S (strong-motion data), T (teleseismic recordings), G (geodetic data), and J (joint) inversions. The numbers in the brackets indicate the number of models in each category, whereas N is the total number of models. The color version of this figure is available only in the electronic edition.

oblique-slip components is, in many cases, neglected. Here, we examine three exceptional oblique-slip events that were excluded from the regression analyses in terms of how they fit into the derived scaling relations (Fig. 10). The 2008 Wenchuan earthquake occurred on a thrust fault, initiated as reverse-faulting rupture, but progressively transitioned into a strike-slip mode (Yagi *et al.*, 2012; Fielding *et al.*, 2013). The estimated rupture dimensions of this event, especially L, follow the scaling laws of strike-slip events. On the other hand, the estimated length L of the 1989 Loma Prieta earthquake agrees with the scaling relationships for reverse-faulting events, whereas the estimated W agrees more with strike-slip events than with reverse-faulting ones. The 1978 Tabas earthquake, although classified as a thrust-faulting earthquake (Hartzell and Mendoza, 1991), reveals a rupture length L consistent with the scaling of strike-slip events, whereas its rupture width W is exceptionally large and does not match with the scaling law. However, the estimated rupture dimensions for this event may be poorly constrained.

An *ad hoc* approach to emulate the scaling of L for oblique-slip events may be to combine the scaling laws for different faulting types with appropriate weights. For instance, strike-slip scaling of L would be more appropriate if rupture grows primarily along strike, involving also strike-slip faulting, as observed during (or in) the Wenchuan earthquake. Also, in the case of steep fault dip ($\delta \geq 70°$), the scaling of W for strike-slip events would be more applicable to account for the restricted growth of W (with increasing M_w), due to the finite seismogenic depth. Thus, we find that the source-scaling laws for the dominant faulting types can be used to describe the source parameters of oblique-slip events.

Scaling of Fault Segments

Large earthquakes, especially those on strike-slip faults, are typically associated with along-strike rupturing of multiple fault segments. The characteristics of fault segments play an important role for rupture propagation and arrest, slip distributions, and source-scaling properties (Manighetti *et al.*, 2005, 2007; Wesnousky, 2006, 2008; Kase, 2010; Wesnousky and Biasi, 2011; Carpenter *et al.*, 2012). Here, we analyze the rupture models for the scaling behavior of their along-strike fault segments in terms of the relationships between segment-specific width W^S, length L^S, area A^S, and moment magnitude M_w^S, calculated for each fault segment individually.

The bulk of rupture models with along-strike segmentation belongs to strike-slip regimes, with 14 events (out of which 13 are continental events). For other faulting regimes, the models available comprise only three reverse-faulting events, a subduction-interface event, and three normal-slip events (two of which occurred at a depth > 50 km). Owing to the data availability, we focus on the continental strike-slip events. As such, along-strike fault segmentation is far more common with strike-slip events compared to other faulting regimes.

Figure 11 illustrates an example for the computation of source parameters specific to each fault segment. We com-

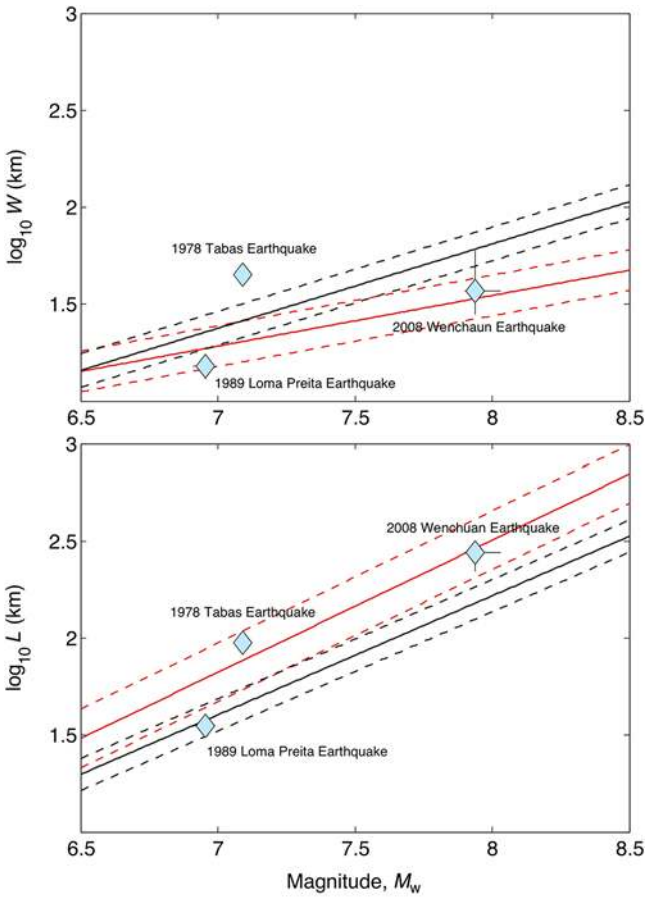

Figure 10. The rupture width and rupture length of three exceptional oblique-slip events compared to the empirical scaling laws for strike-slip events, denoted by the lighter lines, and for reverse-faulting (shallow crust) events, denoted by the darker lines. Note that the scaling law for reverse-faulting events has been extended beyond the upper data limit (Table 1). Interestingly, the 2008 Wenchuan earthquake follows the scaling of strike-slip events. The 1978 Tabas earthquake appears to be an outlier for the rupture width, but it might be that the estimate is poorly constrained. The 1989 Loma Prieta earthquake agrees with the scaling of reverse-faulting events, but its rupture width corresponds to the lower bounds predicted by the scaling laws. The color version of this figure is available only in the electronic edition.

pute effective source dimensions for each fault segment in the same manner as for single-segment rupture models. As discussed previously, the slip distributions generally taper to zero (or very low slip values) at the fault edges. For multi-segment faults, this slip-tapering behavior can be expected at fault segments associated with rupture terminations. Therefore, we classify the fault segment into two groups: (1) exterior (associated with rupture terminations) and (2) interior ones.

Furthermore, we avoid direct regressions (due to the small sample size) and apply both empirical and theoretical constraints on the slope to avoid bias also due to multiple rupture models for the same events. Therefore, we investigate whether the relationships for fault-segment-based source parameters are consistent with those for the entire rupture (i.e., combining all fault segments), or whether they conform to either self-similar scaling or W-model scaling.

Figure 12 shows that the relationships between M_w^S and W^S are very similar to the scaling relationship for the overall rupture width. However, we observe that W^S tends to saturate for larger magnitudes ($M_w^S > 7.0$). On the other hand, the scaling of L^S with respect to M_w^S indicates that fault segments have significantly shorter rupture length (L^S) for a given moment magnitude compared to that given by the scaling law for overall rupture length. Furthermore, for the same M_w^S, exterior fault segments show larger L^S than the interior ones, consistent with slip-tapering behavior at the rupture terminations. However, we find that the scaling of L^S with M_w^S for the interior fault segments is consistent with the W-model scaling (slope ~1.0; Leonard, 2010), in agreement with the saturation of W^S.

Therefore, the scaling behavior is better explained by the relationships between M_w^S and $\log_{10} A^S$. The entire rupture area, for a given magnitude (i.e., $M_w = M_w^S$), is ~1.8 times larger than the exterior fault-segment area (for the same magnitude), and ~3.1 times larger than the interior fault-segment area (for the same magnitude). Thus, fault segments (both exterior and interior) accommodate significantly larger average slips per segment length and, consequently, also over the segment area, compared to the total average slip over the

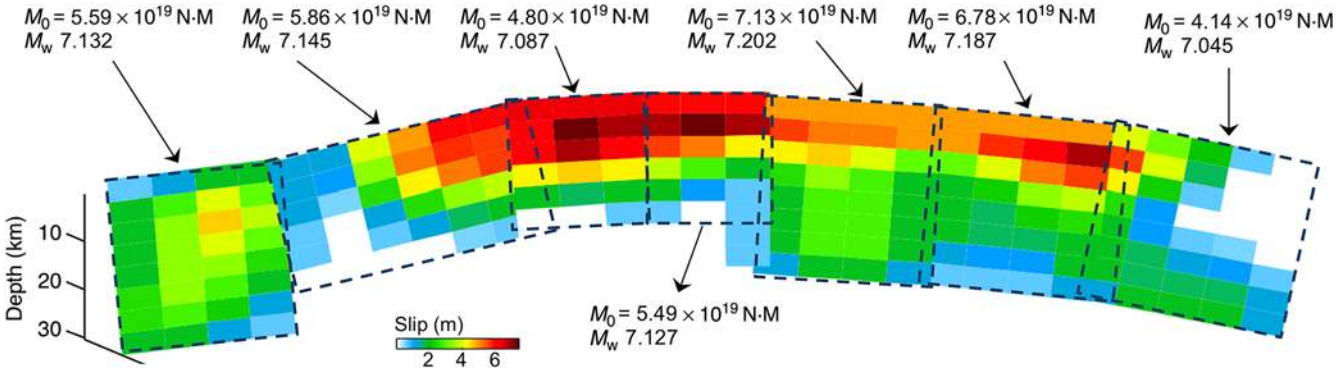

Figure 11. An example depicting the computation of source parameters for the fault segments, using the rupture model given by Avouac *et al.* (2014) for the 2013 Balochistan earthquake. The color version of this figure is available only in the electronic edition.

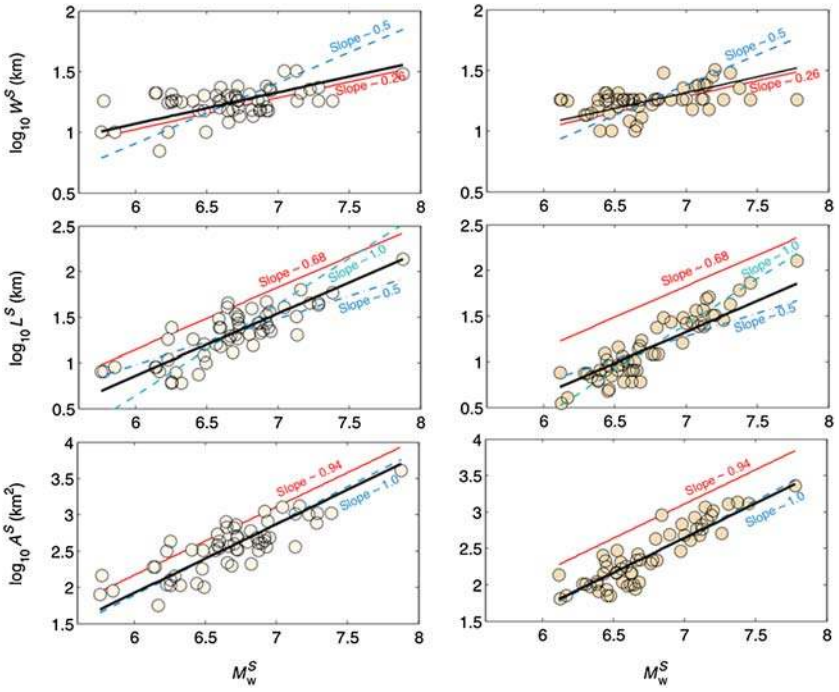

Figure 12. The plots depict the regression analyses for different parameters for exterior fault segments (left column) and interior fault segments (right column). The parameters are fault-segment width W^S, length L^S, area A^S, and moment magnitude M_w^S. The solid lighter lines denote the respective empirical scaling laws for strike-slip events (as listed in Table 1). The darker solid and dashed lines are given by the regressions, with the slope fixed to the empirical scaling laws and self-similar constraints. The dashed-dotted lines on the plots between M_w^S and $\log_{10} L^S$ represent a W-model scaling with slope ~1.0. The relationships between W^S and M_w^S are roughly consistent with that of overall rupture width, but those between L^S and M_w^S, and A^S and M_w^S, are different from the overall scaling laws, with shorter length and smaller area associated with fault segments for the same moment magnitude. The color version of this figure is available only in the electronic edition.

entire fault. One possible explanation for this observation is that segmented faults have higher strength because joints or kinks behave as barriers that require higher stress level to break.

Discussions

Next, we discuss the implications of the proposed scaling laws on earthquake mechanics, focusing on the differences of source-scaling properties and the variability of average stress drop across different faulting regimes. Additionally, we appraise the new empirical scaling laws in terms of their practical applications.

Variability of Source-Scaling Properties

Our analysis reveals that source-scaling properties for different faulting regimes show statistically significant differences (Figs. 4–6). These differences are exhibited through the variability of the average fault-aspect ratio (L/W), as shown in Figure 13. A power-law relationship between L and W is naturally given by the scaling of L and W with respect to M_w, such that $L \propto W^\beta$. Our observed variability in this relationship contradicts with Leonard (2010), who proposed $\beta \sim 1.5$, irrespective of faulting style (except for width-saturated strike-slip events). We observe that the average power-index β varies from 1.4 (for reverse-faulting shallow crustal events) to 1.5 (for normal-faulting events) and from 1.6 (for subduction-interface events) to 2.6 (for strike-slip events).

A consistent observation is that L grows more rapidly than W with increasing M_w. This feature is most prominent for strike-slip events. A possible physical explanation for this observation is nonuniform distribution of frictional resistance (fault strength) and stress concentrations (e.g., Rivera and Kanamori, 2002). The influence of varying fault strength on source-scaling properties has been discussed often (e.g., Das and Scholz, 1983; Strehlau, 1986; Bodin and Brune, 1996; Mai and Beroza, 2000; Shaw and Scholz, 2001; Miller, 2002; Wesnousky, 2006; Lozos *et al.*, 2015). The fault strength tends to increase with depth, which in turn would restrict down-dip seismic slip (Das and Scholz, 1983; Strehlau, 1986). On the other hand, longer ruptures are associated with along-strike zones of low fault strength or high shear stress (Wesnousky, 2006; Lozos *et al.*, 2015).

Another argument for the differences in the scaling of the fault-aspect ratio relates to the finite seismogenic depth and hence is a manifestation of the W-model. The scaling of the fault-aspect ratio correlates with average fault dip, which is steepest for strike-slip events ($\delta \sim 70°$–$90°$) and shallowest for subduction-interface events ($\delta \sim 10°$–$30°$). The impact of seismogenic depth on the scaling relationships would depend on the average fault dip, such that steeper faults are more affected. For events with slip-centroid depth < 50 km, Figure 14 depicts the ratio between $\log_{10} L$ and $\log_{10} W$ (considering a power-law relationship between the two parameters) with respect to fault-dip angles. Ⓔ Figure S14 provides a similar plot but between $\log_{10} L/W$ and fault-dip angles. In general, fault-aspect ratio tends to increase with earthquake magnitude. We consider only large events ($M_w \geq 7.0$) and find an overall positive correlation between the fault-aspect ratio and fault-dip angles; for steeper faults, the aspect ratio is larger. Thus, it could be a combination of these factors (favorably aligned frictional strength and the effects of finite seismogenic depth) that control the scaling of the fault-aspect ratio.

Apart from the differences in the fault-aspect ratio, we find that, for a given magnitude, the subduction-interface

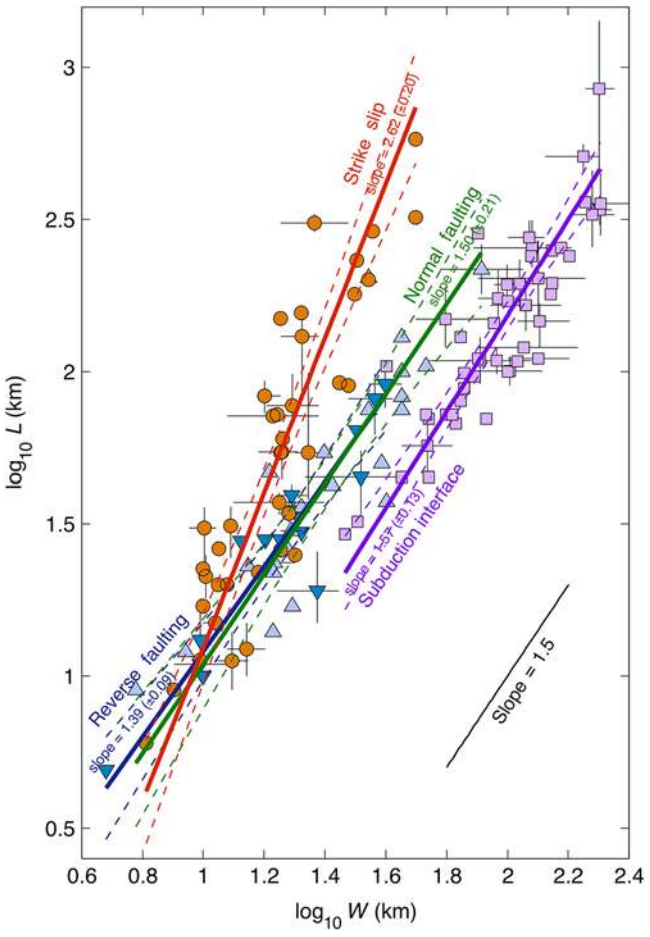

Figure 13. The regression analyses show that the relationship between rupture width W and rupture length L depends on the faulting regime, with variable slope (or power-law index). The gray bars indicate the range of parameter values for events with multiple source models; the logarithmic mean of these values is used in the analysis. The color version of this figure is available only in the electronic edition.

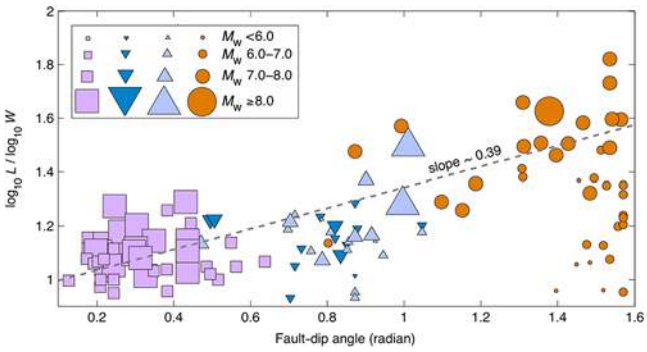

Figure 14. The fault-dip angle and ratio between $\log_{10} L$ and $\log_{10} W$ shows a positive correlation (correlation coefficient ~0.80) for large events ($M_w \geq 7.0$) with slip-centroid depth < 50 km. For this event subset, the linear orthogonal fit (dashed line) also reveals a positive correlation. The symbols and notations are the same as in Figure 4. The color version of this figure is available only in the electronic edition.

events show larger W than other faulting regimes (Fig. 4). Obviously, subduction-interface zones tend to reach larger rupture width, possibly due to the gentle fault dip, relatively higher tectonic stress on the fault indicated by more-frequent seismic activity (e.g., Schorlemmer *et al.*, 2005), and the thermal and structural properties (e.g., Hyndman *et al.*, 1995; Oleskevich *et al.*, 1999).

Another consistent observation is that empirical scaling laws between M_w and A generally agree with self-similar scaling, except for normal-faulting events. As noted earlier, this scaling is consistent with the expectation from a circular shear crack (Kanamori and Anderson, 1975; Hanks and Bakun, 2002). Most of the earlier studies combined reverse and normal dip-slip events into a single faulting regime (e.g., Mai and Beroza, 2000; Henry and Das, 2001; Leonard, 2010; Yen and Ma, 2011). Here, we differentiate between normal and reverse dip-slip earthquakes because these rupture mechanisms are distinctly different, due to the acting tectonic stress regime (reverse faulting: upward dislocation of the hanging wall associated with crustal shortening, and normal faulting: down-dip collapse of the hanging wall resulting in crustal extension). Additionally, normal-faulting earthquakes generally occur on steeper faults ($\delta \sim 50°$–$60°$) compared to reverse-faulting earthquakes ($\delta \sim 40°$–$50°$). Consequently, the variations in source-scaling properties between normal and reverse dip-slip earthquakes are driven by a combination of geometrical effects and acting stresses.

The inhibited growth of W for normal-faulting events is not accompanied by a rapid growth of L, as observed for strike-slip events. However, normal-faulting earthquakes are more often associated with listric faults (for which dip decreases with increasing depth) than with other faulting regimes. In this context, either the scaling relationship for W requires correction for the down-dip geometrical complexity of the fault, or slip is negligible at the deeper parts of listric faults, due to increasingly shallower fault dip (e.g., Williams and Vann, 1987). These aspects warrant further research; however, a few recent studies of listric faults suggest that slip is insignificant at deeper parts of the fault where fault dip is almost horizontal (e.g., Zhang *et al.*, 2010; Fielding *et al.*, 2013; Jolivet *et al.*, 2014).

For strike-slip earthquakes, the expected saturation of W, and hence the proposed W-model scaling, is not observed (e.g., Scholz, 1982; Romanowicz, 1992), although a finite seismogenic depth would predict such behavior. However, there is considerable variation of seismogenic depth globally, depending on the seismotectonics of the region, which could obfuscate any W scaling. Regional variations of seismogenic depth also correlate with observed maximum earthquake magnitude (Martínez-Garzón *et al.*, 2015). It has also been suggested that large strike-slip earthquakes may penetrate deeper than the seismogenic layer, albeit at lower slip rates and with smaller moment release, driven by the particular rupture dynamics (Shaw and Scholz, 2001; Shaw and Wesnousky, 2008; Jiang and Lapusta, 2016). Therefore, W-model scaling may not be immediately apparent for a

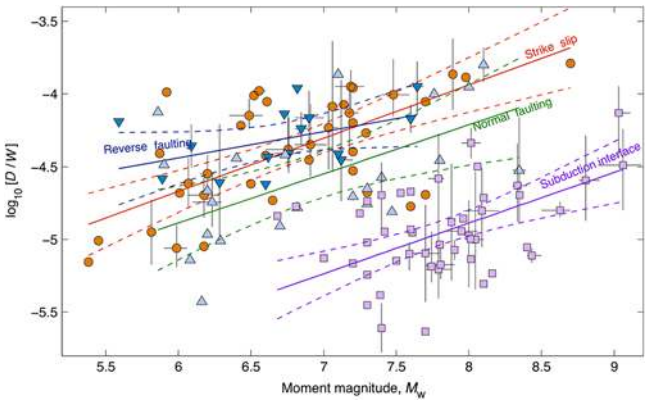

Figure 15. Distribution of average slip D over rupture width W, related to average strain and hence stress drop (Mai and Beroza, 2000), with respect to moment magnitude M_w. Subduction-interface events exhibit the smallest average stress drop. Except for shallow crustal reverse-faulting events, this stress-drop proxy tends to increase with M_w. The color version of this figure is available only in the electronic edition.

global dataset, but it may be discernable at a regional scale. We will return to this aspect in the context of applicability of the scaling laws.

Variability of Average Stress Drop

Our observed source-scaling properties suggest that subduction-interface earthquakes are associated with lower average static-stress drop than earthquakes of other faulting regimes (especially shallow crustal reverse-faulting events). In the case of strike-slip and normal-faulting events, W grows slowly, but D grows faster with increasing M_w, which implies that smaller-magnitude events have lower stress drop than larger earthquakes. The inferred variability of stress drop conforms to the scaling differences between intraplate and interplate earthquakes and also to the dependence of stress drop on the faulting regimes (e.g., Scholz *et al.*, 1986; Mai and Beroza, 2000; Allmann and Shearer, 2009; Konstantinou, 2014).

To investigate the scale dependence of average stress drop, we consider that the static stress drop for a uniform stress-drop shear crack can be defined as

$$\Delta\sigma = C\mu\frac{D}{L_c}, \tag{10}$$

in which L_c is a characteristic length (usually the smallest dimension, hence typically W) of the earthquake, and C is a constant of order unity (Kanamori and Anderson, 1975). However, the length scales controlling $\Delta\sigma$ for the actual rupture (also as imaged by the source inversions) are expected to be shorter than the length or width of the entire rupture, owing to the spatially variable slip. Therefore, $\Delta\sigma$ given by equation (10) serves as an approximation for understanding source-scaling properties but not as an accurate measure of the stress change occurring during the earthquake.

Figure 15 depicts distributions of D/W over M_w for the different faulting types; the quantity D/W is related to the strain change and is regarded as a proxy for $\Delta\sigma$ (equation 10). We find that, for the reverse-faulting events, D/W is almost independent of M_w, indicating scale-invariant $\Delta\sigma$. The figure also provides strong evidence of lower $\Delta\sigma$ for subduction-interface events compared to other faulting types. At the same time, we observe an apparent increase of the stress-drop proxy with magnitude. However, this pattern could be due to the paucity of data at higher magnitude ($M_w > 8.5$). Furthermore, considerable variability exists for $\Delta\sigma$ across different subduction zones and even across different segments of a subduction interface (e.g., Seno, 2014). Thus, the scale-invariance property of $\Delta\sigma$ for subduction-interface events cannot be concluded.

We remark that Bilek and Lay (1999) observed that the constant stress drop of earthquakes in subduction zones can be derived by considering the depth variability of crustal rigidity. Ripperger and Mai (2004) also discussed the effect of depth-dependent rigidity, such that absolute stress changes decrease in the uppermost low-strength part of the fault. More recently, Ye *et al.* (2016) considered depth-dependent rigidity in source inversions for megathrust events in subduction zones. They observed that $\Delta\sigma$ associated with subduction-interface events does not correlate with earthquake magnitude. Thus, there are complications in relating slip, stress drop, and seismic moment, especially for near-surface rupture in subduction zones in which the rigidity could be significantly small.

On the other hand, a positive correlation can be observed between the stress-drop proxy and magnitude for the normal-faulting and strike-slip events. In the case of normal-faulting events, this positive correlation provides strong evidence of increasing $\Delta\sigma$ and could be related to the restricted growth of W with M_w. This inference is in line with observations of $\Delta\sigma$ increasing with M_w made by recent studies on normal-faulting earthquakes (e.g., Calderoni *et al.*, 2013; Konstantinou, 2014; Pacor *et al.*, 2016).

It is also important to note that the free-surface effect (when the rupture is close to the free surface) may cause relatively large slip, especially for ruptures on near-vertical faults (Archuleta and Frazier, 1978; Brune and Anooshehpoor, 1998; Shi *et al.*, 2003). Such cases can be accounted for using a mirror image of the slip distribution above the free surface (Steketee, 1958) in the stress-change calculations, which results in small stress differences of 1%–2% (Ripperger and Mai, 2004).

Based on the fundamental relationship between magnitude and radiated energy, Kanamori and Riviera (2004) argued that stress drop is necessarily scale-dependent. Previously, Mai and Beroza (2000) reported that scale-dependent behavior of the average stress drop for strike-slip events could be gleaned from a small database of rupture models. Abercrombie and Rice (2005) also observed that stress drop increases slightly with earthquake size. Mai *et al.* (2006) made similar observations based on dynamic rupture

simulations. Likewise, Dalguer *et al.* (2008) studied dynamic simulations and reported that the average stress drop is independent of earthquake size for buried earthquakes but scale-dependent for surface-rupturing earthquakes. From assessment of kinematic rupture models, Causse *et al.* (2014) also observed that stress drop tends to increase with magnitude. More recently, Archuleta and Ji (2016) also suggested possible weak scaling of stress drop with earthquake magnitude.

The scale-dependent $\Delta\sigma$ can be linked to the scaling of D, such that it increases with L and therefore complies with L-model scaling. It has been suggested that large ruptures on long and narrow faults require higher stress drop to propagate (Heaton, 1990; Mai and Beroza, 2000). Our observation of a larger D, and therefore a larger $\Delta\sigma$, within fault segments compared to single-segment rupture (Fig. 12) supports this conjecture. Dynamic rupture simulations also indicate that fault interactions (e.g., ruptures on multiple fault segments) result in higher $\Delta\sigma$ at each fault segment (Kase, 2010). However, we note that if W saturates, then the scaling of L becomes more consistent with the W model, weakening the correlation between D and L.

Average stress drop is strongly connected with source-scaling properties: a constant or scale-invariant $\Delta\sigma$ implies self-similar earthquake source-scaling. Our result of $\Delta\sigma$ being positively correlated with M_w is consistent with observed departures from self-similar earthquake scaling. This scale-dependent behavior implies an upper limit of average stress drop, once the maximum possible magnitude is reached for a given fault system. On the other hand, the inferred variability of $\Delta\sigma$ across different faulting regimes may indicate corresponding differences in the slip heterogeneity (Liu-Zeng *et al.*, 2005), the underlying fault strength and roughness of the fault surface (Miller, 2002; Candela *et al.*, 2011), and the slip-accumulation rate (Anderson *et al.*, 1996). These factors may be interrelated and are being actively investigated (e.g., Zielke *et al.*, 2017).

Applying the Scaling Laws

Let us focus now on the practical aspects of empirical scaling laws. Owing to the use of GORs, our relationships are invariant under the interchange of variables. Therefore, the same relationship can be applied to predict either of the two variables; for instance, $\log_{10} L$ can be predicted from M_w and likewise M_w from $\log_{10} L$.

In deciding a specific relationship, it is important to consider not only the underlying faulting regimes but also the applicable data range (magnitude, length, width, and area) listed in Table 1. However, for smaller magnitudes that are not well represented in the database used in this study (approximately $M_w < 5.5$ for strike-slip, normal-faulting, and reverse-faulting earthquakes and $M_w < 7.0$ for subduction-interface earthquakes), we suggest that self-similar scaling is applicable, based on $M_w - \log_{10} A$ (e.g., Kanamori and Anderson, 1975).

We find that an important discriminating feature between shallow crustal reverse-faulting events and subduction-interface events is the average fault dip. The average fault dip is significantly shallower in the former faulting regime (Figs. 1 and 14). This distinction is important in deciding the pertinent scaling laws.

For megathrust ($M_w > 8.5$) subduction events, potential constraints of finite seismogenic depth on the down-dip rupture width can be achieved by adopting higher confidence on the scaling relationship between M_w and $\log_{10} A$, thereby overruling the scaling between M_w and $\log_{10} L$. In light of the remarkable 2011 Tohoku earthquake, the possibility of very high $\Delta\sigma$ may be considered (taking into account subduction geometry, convergence rate, age, and temperature of the subducting plate; Fry and Ma, 2016). Accordingly, the scaling laws for shallow crustal reverse-faulting events or those given by Goda *et al.* (2016) for tsunamigenic events could be applied to predict exceptionally large M_w from smaller rupture dimensions (or vice versa), in combination with those for subduction-interface events using suitable weights.

For strike-slip earthquakes, the empirical relationship between M_w and $\log_{10} L$ is more consistent with the L model and would allow for more-conservative estimates of M_w from L. However, for the regions where the distribution of seismogenic depth is well established (e.g., Nazareth and Hauksson, 2004) and the upper limit of W can be fixed, the scaling relationship between M_w and $\log_{10} A$ can be applied. With increasing M_w, the scaling of L becomes more aligned to the W model (e.g., Leonard, 2010). This consideration also applies to the scaling of fault segments associated with strike-slip events.

Conclusions

We developed new empirical scaling laws for earthquake-rupture geometry based on a large database of finite-fault rupture models, containing earthquake source models over a wide magnitude range (from M_w 5.4 to 9.2). Our study provides important updates on earthquake source-scaling laws, addressing a primary concern for improving seismic–tsunami-hazard analysis and engineering applications.

Being empirical, the scaling laws preserve the complexities manifested by the data and allow correspondingly for physical interpretations. We observe that rupture length grows more rapidly with magnitude compared to rupture width. On the other hand, subduction-interface earthquakes have significantly larger rupture width (and therefore rupture area), compared to other faulting regimes. On the global scale, the saturation of rupture width is not evident with large strike-slip earthquakes, but inhibited growth of rupture width with magnitude can be perceived. In this case, rupture length exhibits a scaling behavior that is implied by the L model. However, at regional scales for which seismogenic depth is more or less fixed, the scaling behavior close to the W model can be expected. In general, the scaling of rupture area agrees

with self-similar scaling behavior, except for normal-faulting events. Interestingly, the scaling laws imply a strong likelihood of scale-dependent average stress drop, especially with normal-faulting and strike-slip events.

Finally, we note that there are statistically significant differences among the source-scaling properties of the different faulting regimes. Such differences are consistent with the variability of geological and seismological factors (e.g., fault dip, fault strength, stress drop, and rupture mechanics) across different faulting regimes.

Data and Resources

The rupture models used in this study were extracted from the SRCMOD database (http://equake-rc.info/srcmod, last accessed December 2016). The dataset provided by Blaser *et al.* (2010) is available in the electronic supplement to their article.

Acknowledgments

We are thankful to all our colleagues for sharing their rupture models with the SRCMOD database. It is due to their generosity that the present and similar studies are possible. Careful and constructive comments by Shiro Hirano and two anonymous reviewers helped improve the article. The research presented in this article is supported by King Abdullah University of Science and Technology (KAUST) in Thuwal, Saudi Arabia, by Grants BAS/1/1339-01-1 and URF/1/2160-01-01.

References

Abercrombie, R. E., and J. R. Rice (2005). Can observations of earthquake scaling constrain slip weakening?, *Geophys. J. Int.* **162,** 406–424.

Aki, K. (1966). Generation and propagation of G waves from the Niigata earthquake of June 16, 1964: Part 2. Estimation of earthquake moment, released energy and stress drop from the G wave spectra, *Bull. Earthq. Res. Inst., Univ. Tokyo* **44,** 73–88.

Allmann, B. B., and P. M. Shearer (2009). Global variations of stress drop for moderate to large earthquakes, *J. Geophys. Res.* **114,** no. B1, doi: 10.1029/2008JB005821.

Anderson, J. G., S. G. Wesnousky, and M. W. Stirling (1996). Earthquake size as a function of fault slip rate, *Bull. Seismol. Soc. Am.* **86,** 683–690.

Archuleta, R. J., and G. A. Frazier (1978). Three-dimensional numerical simulation of dynamic faulting in a half-space, *Bull. Seismol. Soc. Am.* **68,** 541–572.

Archuleta, R. J., and C. Ji (2016). Moment rate scaling for earthquakes 3.3 ≤ M ≤5.3 with implications for stress drop, *Geophys. Res. Lett.* **43,** 12,004–12,011, doi: 10.1002/2016GL071433.

Avouac, J. P., F. Ayoub, S. Wei, J. P. Ampuero, L. Meng, S. Leprince, R. Jolivet, Z. Duputel, and D. Helmberger (2014). The 2013, M_w 7.7 Balochistan earthquake, energetic strike-slip reactivation of a thrust fault, *Earth Planet. Sci. Lett.* **391,** 128–134.

Beresnev, I. A. (2003). Uncertainties in finite-fault slip inversions: To what extent to believe? (A critical review), *Bull. Seismol. Soc. Am.* **93,** 2445–2458.

Bilek, S. L., and T. Lay (1999). Rigidity variations with depth along interplate megathrust faults in subduction zones, *Nature* **400,** 443–446.

Blaser, L., F. Krüger, M. Ohrnberger, and F. Scherbaum (2010). Scaling relations of earthquake source parameter estimates with special focus on subduction environment, *Bull. Seismol. Soc. Am.* **100,** 2914–2926.

Bodin, P., and J. N. Brune (1996). On the scaling of slip with rupture length for shallow strike-slip earthquakes: Quasistatic models and dynamic rupture propagation, *Bull. Seismol. Soc. Am.* **86,** 1292–1299.

Bonilla, M. G., R. K. Mark, and J. J. Lienkaemper (1984). Statistical relations among earthquake magnitude, surface rupture length, and surface fault displacement, *Bull. Seismol. Soc. Am.* **74,** 2379–2411.

Brune, J. N., and A. Anooshehpoor (1998). A physical model of the effect of a shallow weak layer on strong ground motion for strike-slip ruptures, *Bull. Seismol. Soc. Am.* **88,** 1070–1078.

Calderoni, G., A. Rovelli, and S. K. Singh (2013). Stress drop and source scaling of the 2009 April L'Aquila earthquakes, *Geophys. J. Int.* **192,** 260–274.

Candela, T., F. Renard, M. Bouchon, J. Schmittbuhl, and E. E. Brodsky (2011). Stress drop during earthquakes: Effect of fault roughness scaling, *Bull. Seismol. Soc. Am.* **101,** 2369–2387.

Carpenter, N. S., S. J. Payne, and A. L. Schafer (2012). Toward reconciling magnitude discrepancies estimated from paleoearthquake data, *Seismol. Res. Lett.* **83,** 555–565.

Carroll, R. J., and D. Ruppert (1996). The use and misuse of orthogonal regression estimation in linear errors-in-variables models, *Am. Stat.* **50,** 1–6.

Castellaro, S., F. Mulargia, and Y. Y Kagan (2006). Regression problems for magnitudes, *Geophys. J. Int.* **165,** 913–930.

Causse, M., L. A. Dalguer, and P. M. Mai (2014). Variability of dynamic source parameters inferred from kinematic models of past earthquakes, *Geophys. J Int.* **196,** 1754–1769.

Dalguer, L. A., H. Miyake, S. M. Day, and K. Irikura (2008). Surface rupturing and buried dynamic-rupture models calibrated with statistical observations of past earthquakes, *Bull. Seismol. Soc. Am.* **98,** 1147–1161.

Das, S., and C. Scholz (1983). Why large earthquakes do not nucleate at shallow depths, *Nature* **305,** 621–623.

De Risi, R., and K. Goda (2016). Probabilistic earthquake-tsunami multihazard analysis: Application to the Tohoku region, Japan, *Front. Built Environ.* **2,** Article Number 25, doi: 10.3389/fbuil.2016.00025.

Efron, B. (1982). *The Jackknife, the Bootstrap, and Other Resampling Plans*, Society for Industrial and Applied Mathematics, Philadelphia, Pennsylvania, doi: 10.1137/1.9781611970319.

Fielding, E. J., A. Sladen, Z. Li, J.-P. Avouac, R. Bürgmann, and I. Ryder (2013). Kinematic fault slip evolution source models of the 2008 M 7.9 Wenchuan earthquake in China from SAR interferometry, GPS and teleseismic analysis and implications for Longmen Shan tectonics, *Geophys. J. Int.* **194,** no. 2, 1138–1166, doi: 10.1093/gji/ggt155.

Fry, B., and K. F. Ma (2016). Implications of the great M_w 9.0 Tohoku-Oki earthquake on the understanding of natural hazard in Taiwan and New Zealand, *Seismol. Res. Lett.* **87,** 1254–1258.

Fuller, W. A. (1987). *Measurement Error Models*, John Wiley & Sons, New York, New York.

Galvez, P., L. A. Dalguer, J. P. Ampuero, and D. Giardini (2016). Rupture reactivation during the 2011 M_w 9.0 Tohoku earthquake: Dynamic rupture and ground-motion simulations, *Bull. Seismol. Soc. Am.* **106,** 819–831.

Geller, R. J. (1976). Scaling relations for earthquake source parameters and magnitudes, *Bull. Seismol. Soc. Am.* **66,** 1501–1523.

Ghasemi, A., and S. Zahediasl (2012). Normality tests for statistical analysis: A guide for non-statisticians, *Int. J. Endocrinol. Metab.* **10,** 486–489.

Goda, K., T. Yasuda, N. Mori, and T. Maruyama (2016). New scaling relationships of earthquake source parameters for stochastic tsunami simulation, *Coast. Eng. J.* **58,** no. 3, 1650010, doi: 10.1142/S0578563416500108.

Gomberg, J., A. Wech, K. Creager, K. Obara, and D. Agnew (2016). Reconsidering earthquake scaling, *Geophys. Res. Lett.* **43,** 6243–6251, doi: 10.1002/2016GL069967.

Hanks, T. C., and W. H. Bakun (2002). A bilinear source-scaling model for M-log *A* observations of continental earthquakes, *Bull. Seismol. Soc. Am.* **92,** 1841–1846.

Hanks, T. C., and W. H. Bakun (2008). M-log *A* observations of recent large earthquakes, *Bull. Seismol. Soc. Am.* **98,** 490–494.

Hanks, T. C., and H. Kanamori (1979). A moment magnitude scale, *J. Geophys. Res.* **84,** no. B5, 2348–2350, doi: 10.1029/JB084iB05p02348.

Hartzell, S., and C. Mendoza (1991). Application of an iterative least-squares waveform inversion of strong-motion and teleseismic records to the 1978 Tabas, Iran, earthquake, *Bull. Seismol. Soc. Am* **81,** no. 2, 305–331.

Heaton, T. H. (1990). Evidence for and implications of self-healing pulses of slip in earthquake rupture, *Phys. Earth Planet. In.* **64,** 1–20.

Henry, C., and S. Das (2001). Aftershock zones of large shallow earthquakes: Fault dimensions, aftershock area expansion and scaling relations, *Geophys. J. Int.* **147,** 272–293.

Henry, C., S. Das, and J. H. Woodhouse (2000). The great March 25, 1998, Antarctic Plate earthquake: Moment tensor and rupture history, *J. Geophys. Res.* **105,** 16,097–16,119.

Herrendörfer, R., Y. van Dinther, T. Gerya, and L. A. Dalguer (2015). Earthquake supercycle in subduction zones controlled by the width of the seismogenic zone, *Nature Geosci.* **8,** 471–474.

Hyndman, R. D., K. Wang, and M. Yamano (1995). Thermal constraints on the seismogenic portion of the southwestern Japan subduction thrust, *J. Geophys. Res.* **100,** 15,373–15,392.

Jiang, J., and N. Lapusta (2016). Deeper penetration of large earthquakes on seismically quiescent faults, *Science* **352,** 1293–1297.

Johnston, A. C., and L. R. Kanter (1990). Stable continental earthquakes, *Sci. Am.* **262,** 68–75.

Jolivet, R., Z. Duputel, B. Riel, M. Simons, L. Rivera, S. E. Minson, H. Zhang, M. A. G. Aivazis, F. Ayoub, S. Leprince, *et al.* (2014). The 2013 M_w 7.7 Balochistan earthquake: Seismic potential of an accretionary wedge, *Bull. Seismol. Soc. Am.* **104,** 1020–1030.

Kanamori, H., and D. L. Anderson (1975). Theoretical basis of some empirical relations in seismology, *Bull. Seismol. Soc. Am.* **65,** 1073–1095.

Kanamori, H., and K. C. McNally (1982). Variable rupture mode of the subduction zone along the Ecuador–Colombia coast, *Bull. Seismol. Soc. Am.* **72,** 1241–1253.

Kanamori, H., and L. Rivera (2004). Static and dynamic scaling relations for earthquakes and their implications for rupture speed and stress drop, *Bull. Seismol. Soc. Am.* **94,** 314–319.

Kase, Y. (2010). Slip-length scaling law for strike-slip multiple segment earthquakes based on dynamic rupture simulations, *Bull. Seismol. Soc. Am.* **100,** 473–481.

King, G. C., and S. G. Wesnousky (2007). Scaling of fault parameters for continental strike-slip earthquakes, *Bull. Seismol. Soc. Am.* **97,** 1833–1840.

Konstantinou, K. I. (2014). Moment magnitude-rupture area scaling and stress-drop variations for earthquakes in the Mediterranean region, *Bull. Seismol. Soc. Am.* **104,** 2378–2386.

Konstantinou, K. I., G. A. Papadopoulos, A. Fokaefs, and K. Orphanogiannaki (2005). Empirical relationships between aftershock area dimensions and magnitude for earthquakes in the Mediterranean sea region, *Tectonophysics* **403,** 95–115.

Lee, S.-J., B.-S. Huang, M. Ando, H.-C. Chiu, and J.-H. Wang (2011). Evidence of large scale repeating slip during the 2011 Tohoku-Oki earthquake, *Geophys. Res. Lett.* **38,** L19306, doi: 10.1029/2011GL049580.

Leonard, M. (2010). Earthquake fault scaling: Relating rupture length, width, average displacement, and moment release, *Bull. Seismol. Soc. Am.* **100,** 1971–1988.

Leonard, M. (2014). Self-consistent earthquake fault-scaling relations: Update and extension to stable continental strike-slip faults, *Bull. Seismol. Soc. Am.* **104,** 2953–2965.

Lilliefors, H. W. (1967). On the Kolmogorov–Smirnov test for normality with mean and variance unknown, *J. Am. Stat. Assoc.* **62,** 399–402.

Liu-Zeng, J., T. Heaton, and C. DiCaprio (2005). The effect of slip variability on earthquake slip-length scaling, *Geophys. J. Int.* **162,** 841–849.

Llenos, A. L., and J. J. McGuire (2007). Influence of fore-arc structure on the extent of great subduction zone earthquakes, *J. Geophys. Res.* **112,** no. B09301, doi: 10.1029/2007JB004944.

Lozos, J. C., D. D. Oglesby, J. N. Brune, and K. B. Olsen (2015). Rupture and ground-motion models on the northern San Jacinto fault, incorporating realistic complexity, *Bull. Seismol. Soc. Am.* **105,** 1931–1946.

Mai, P. M., and G. C. Beroza (2000). Source scaling properties from finite-fault-rupture models, *Bull. Seismol. Soc. Am.* **90,** 604–615.

Mai, P. M., and K. K. S. Thingbaijam (2014). SRCMOD: An online database of finite-fault rupture models, *Seismol. Res. Lett.* **85,** 1348–1357.

Mai, P. M., J. Burjanek, B. Delouis, G. Festa, C. Francois-Holden, D. Monelli, T. Uchide, and J. Zahradnik (2007). Earthquake source inversion blindtest: Initial results and further developments, *Eos Trans. AGU* **88,** no. 52 (Fall Meet. Suppl.), Abstract S53C-08.

Mai, P. M., D. Schorlemmer, M. Page, J.-P. Ampuero, K. Asano, M. Causse, S. Custodio, W. Fan, G. Festa, M. Galis, *et al.* (2016). The earthquake-source inversion validation (SIV) project, *Seismol. Res. Lett.* **87,** no. 3, 690–708, doi: 10.1785/0220150231.

Mai, P. M., P. Somerville, A. Pitarka, L. Dalguer, S. Song, G. Beroza, H. Miyake, and K. Irikura (2006). On scaling of fracture energy and stress drop in dynamic rupture models: Consequences for near-source ground-motions, in *Earthquakes: Radiated Energy and the Physics of Faulting*, R. Abercrombie, A. McGarr, H. Kanamori, and G. Di Toro (Editors), Geophysical Monograph Series, Vol. 170, American Geophysical Union, 283–293.

Mai, P. M., P. Spudich, and J. Boatwright (2005). Hypocenter locations in finite-source rupture models, *Bull. Seismol. Soc. Am.* **95,** 965–980.

Manighetti, I., M. Campillo, S. Bouley, and F. Cotton (2007). Earthquake scaling, fault segmentation, and structural maturity, *Earth Planet. Sci. Lett.* **253,** 429–438.

Manighetti, I., M. Campillo, C. Sammis, P. M. Mai, and G. King (2005). Evidence for self-similar, triangular slip distributions on earthquakes: Implications for earthquake and fault mechanics, *J. Geophys. Res.* **110,** no. B05302, doi: 10.1029/2004JB003174.

Martínez-Garzón, P., M. Bohnhoff, Y. Ben-Zion, and G. Dresen (2015). Scaling of maximum observed magnitudes with geometrical and stress properties of strike-slip faults, *Geophys. Res. Lett.* **42,** no. 23, 10,230–10,238, doi: 10.1002/2015GL066478.

Miller, S. A. (2002). Earthquake scaling and the strength of seismogenic faults, *Geophys. Res. Lett.* **29,** no. 10, 27-1–27-4, doi: 10.1029/2001GL014181.

Murotani, S., H. Miyake, and K. Koketsu (2008). Scaling of characterized slip models for plate-boundary earthquakes, *Earth Planets Space* **60,** 987–991.

Murotani, S., K. Satake, and Y. Fujii (2013). Scaling relations of seismic moment, rupture area, average slip, and asperity size for M ~ 9 subduction-zone earthquakes, *Geophys. Res. Lett.* **40,** 5070–5074.

Nazareth, J. J., and E. Hauksson (2004). The seismogenic thickness of the southern California crust, *Bull. Seismol. Soc. Am.* **94,** 940–960.

Oleskevich, D. A., R. D. Hyndman, and K. Wang (1999). The updip and downdip limits to great subduction earthquakes: Thermal and structural models of Cascadia, south Alaska, SW Japan, and Chile, *J. Geophys. Res.* **104,** 14,965–14,991.

Pacheco, J. F., L. R. Sykes, and C. H. Scholz (1993). Nature of seismic coupling along simple plate boundaries of the subduction type, *J. Geophys. Res.* **98,** no. B8, 14,133–14,159, doi: 10.1029/93JB00349.

Pacor, F., D. Spallarossa, A. Oth, L. Luzi, R. Puglia, L. Cantore, A. Mercuri, M. D'Amico, and D. Bindi (2016). Spectral models for ground motion prediction in the L'Aquila region (central Italy): Evidence for stress-drop dependence on magnitude and depth, *Geophys. J. Int.* **204,** 697–718.

Page, M. T., S. Custódio, R. J. Archuleta, and J. M. Carlson (2009). Constraining earthquake source inversions with GPS data: 1. Resolution-based removal of artifacts, *J. Geophys. Res.* **114,** no. B01314, doi: 10.1029/2007JB005449.

Papazachos, B. C., E. M. Scordilis, D. G. Panagiotopoulos, C. B. Papazachos, and G. F. Karakaisis (2004). Global relations between seismic fault parameters and moment magnitudes of earthquakes, *Bull. Geol. Soc. Greece* **36,** 1482–1489.

Pegler, G., and S. Das (1996). Analysis of the relationship between seismic moment and fault length for large crustal strike-slip earthquakes between 1977–1992, *Geophys. Res. Lett.* **23,** 905–908.

Ramírez-Gaytán, A., J. Aguirre, M. A. Jaimes, and V. Huérfano (2014). Scaling relationships of source parameters of M_w 6.9–8.1 earthquakes

in the Cocos–Rivera–North American subduction zone, *Bull. Seismol. Soc. Am.* **104,** 840–854.

Ripperger, J., and P. M. Mai (2004). Fast computation of static stress changes on 2D faults from final slip distributions, *Geophys. Res. Lett.* **31,** L18610, doi: 10.1029/2004GL020594.

Rivera, L., and H. Kanamori (2002). Spatial heterogeneity of tectonic stress and friction in the crust, *Geophys. Res Lett.* **29,** no. 6, doi: 10.1029/2001GL013803.

Rodríguez-Pérez, Q., and L. Ottemöller (2013). Finite-fault scaling relations in Mexico, *Geophys. J. Int.* **193,** 1570–1588.

Romanowicz, B. (1992). Strike-slip earthquakes on quasi-vertical transcurrent faults: Inferences for general scaling relations, *Geophys. Res. Lett.* **19,** 481–484.

Romanowicz, B., and L. J. Ruff (2002). On moment-length scaling of large strike slip earthquakes and the strength of faults, *Geophys. Res. Lett.* **29,** no. 12, doi: 10.1029/2001GL014479.

Scholz, C. H. (1982). Scaling laws for large earthquakes: Consequences for physical models, *Bull. Seismol. Soc. Am.* **72,** 1–14.

Scholz, C. H. (1994). A reappraisal of large earthquake scaling, *Bull. Seismol. Soc. Am.* **84,** 215–218.

Scholz, C. H. (2002). *The Mechanics of Earthquakes and Faulting*, Cambridge University Press, Cambridge, United Kingdom.

Scholz, C. H., C. A. Aviles, and S. G. Wesnousky (1986). Scaling differences between large interplate and large intraplate earthquakes, *Bull. Seismol. Soc. Am.* **76,** 65–70.

Schorlemmer, D., S. Wiemer, and M. Wyss (2005). Variations in earthquake-size distribution across different stress regimes, *Nature* **437,** 539–542.

Seno, T. (2014). Stress drop as a criterion to differentiate subduction zones where M_w 9 earthquakes can occur, *Tectonophysics* **621,** 198–210.

Shapiro, S. S., and M. B. Wilk (1965). An analysis of variance test for normality (complete samples), *Biometrika* **52,** 591–611.

Shaw, B. E. (2009). Constant stress drop from small to great earthquakes in magnitude-area scaling, *Bull. Seismol. Soc. Am.* **99,** 871–875.

Shaw, B. E., and C. H. Scholz (2001). Slip-length scaling in large earthquakes: Observations and theory and implications for earthquake physics, *Geophys. Res. Lett.* **28,** no. 15, 2995–2998, doi: 10.1029/2000GL012762.

Shaw, B. E., and S. G. Wesnousky (2008). Slip-length scaling in large earthquakes: The role of deep penetrating slip below the seismogenic layer, *Bull. Seismol. Soc. Am.* **98,** 1633–1641.

Shi, B., J. N. Brune, Y. Zeng, and A. Anooshehpoor (2003). Dynamics of earthquake normal faulting: Two-dimensional lattice particle model, *Bull. Seismol. Soc. Am.* **93,** 1179–1197.

Skarlatoudis, A. A., P. G. Somerville, and H. K. Thio (2016). Source-scaling relations of interface subduction earthquakes for strong ground motion and tsunami simulation, *Bull. Seismol. Soc. Am.* **106,** no. 4, 1652, doi: 10.1785/0120150320.

Somerville, P. G., K. Irikura, R. Graves, S. Sawada, D. Wald, N. Abrahamson, Y. Iwasaki, T. Kagawa, N. Smith, and A. Kowada (1999). Characterizing crustal earthquake slip models for the prediction of strong ground motion, *Seismol. Res. Lett.* **70,** 59–80.

Stafford, P. J. (2014). Source-scaling relationships for the simulation of rupture geometry within probabilistic seismic-hazard analysis, *Bull. Seismol. Soc. Am.* **104,** 1620–1635.

Steketee, J. A. (1958). On Volterra's dislocation in a semi-infinite elastic medium, *Can. J. Phys.* **36,** 192–205.

Stirling, M., T. Goded, K. Berryman, and N. Litchfield (2013). Selection of earthquake scaling relationships for seismic-hazard analysis, *Bull. Seismol. Soc. Am.* **103,** 2993–3011.

Stock, S., and E. G. C. Smith (2000). Evidence for different scaling of earthquake source parameters for large earthquakes depending on fault mechanism, *Geophys. J. Int.* **143,** 157–162.

Strasser, F. O., M. C. Arango, and J. J. Bommer (2010). Scaling of the source dimensions of interface and intraslab subduction-zone earthquakes with moment magnitude, *Seismol. Res. Lett.* **81,** 941–950.

Strehlau, J. (1986). A discussion of the depth extent of rupture in large continental earthquakes, in *Earthquake Source Mechanism*, S. Das, J. Boatwright, and C. H. Scholz (Editors), Geophysical Monograph Series, Vol. 37, American Geophysical Union, 131–145.

Thingbaijam, K. K. S., and P. M. Mai (2016). Evidence for truncated exponential probability distribution of earthquake slip, *Bull. Seismol. Soc. Am.* **106,** 1802–1816.

Wells, D. L., and K. J. Coppersmith (1994). New empirical relationships among magnitude, rupture length, rupture width, rupture area, and surface displacement, *Bull. Seismol. Soc. Am.* **84,** 974–1002.

Wesnousky, S. G. (2006). Predicting the endpoints of earthquake ruptures, *Nature* **444,** 358–360.

Wesnousky, S. G. (2008). Displacement and geometrical characteristics of earthquake surface ruptures: Issues and implications for seismic-hazard analysis and the process of earthquake rupture, *Bull. Seismol. Soc. Am.* **98,** no. 4, 1609–1632.

Wesnousky, S. G., and G. P. Biasi (2011). The length to which an earthquake will go to rupture, *Bull. Seismol. Soc. Am.* **101,** no. 4, 1948–1950.

Williams, G. D., and I. Vann (1987). The geometry of listric normal faults and deformation in the hanging walls, *J. Struct. Geol.* **9,** 789–795.

Yagi, Y., N. Nishimura, and A. Kasahara (2012). Source process of the 12 May 2008 Wenchuan, China, earthquake determined by waveform inversion of teleseismic body waves with a data covariance matrix, *Earth Planets Space* **64,** e13–e16.

Ye, L., T. Lay, H. Kanamori, and L. Rivera (2016). Rupture characteristics of major and great ($M_w \geq 7.0$) megathrust earthquakes from 1990 to 2015: 1. Source parameter scaling relationships, *J. Geophys. Res.* **121,** 826–844, doi: 10.1002/2015JB012426.

Yen, Y.-T., and K.-F. Ma (2011). Source-scaling relationship for M 4.6–8.1 earthquakes, specifically for earthquakes in the collision zone of Taiwan, *Bull. Seismol. Soc. Am.* **101,** 464–481.

Yen, Y.-T., K.-F. Ma, and Y.-Y. Wen (2008). Slip partition of the 26 December 2006 Pingtung, Taiwan (M 6.9, M 6.8) earthquake doublet determined from teleseismic waveforms, *Terr. Atmos. Ocean. Sci.* **19,** 567–578.

Yue, H., T. Lay, and K. D. Koper (2012). *En echelon* and orthogonal fault ruptures of the 11 April 2012 great intraplate earthquakes, *Nature* **490,** 245–249.

Zhang, P., X. Wen, Z.-K. Shen, and J. Chen (2010). Oblique, high-angle, listric-reverse faulting and associated development of strain: The Wenchuan earthquake of May 12, 2008, Sichuan, China. *Ann. Rev. Earth Planet. Sci.* **38,** 353–382.

Zhou, S., K. Irikura, and X. Chen (2004). Analysis of the reliability and resolution of the earthquake source history inferred from waveforms, taking the Chi-Chi earthquake as an example, *Geophys. J. Int.* **157,** no. 3, 1217–1232.

Zielke, O., M. Galis, and P. M. Mai (2017). Fault roughness and strength heterogeneity control earthquake size and stress drop, *Geophys. Res. Lett.* **44,** 777–783.

Appendix

Scaling of Continental Strike-Slip Earthquakes

Figure A1 shows the regression between M_w and $\log_{10} L$ using the entire dataset for continental strike-slip earthquakes, which appears to follow $M_0 \propto L^2$ scaling (according to the obtained fit with slope ~0.68). On the other hand, W grows very slowly with increasing M_w. Residuals do not show any systematic trends, and the statistical tests do not reject their normality.

In Figure A2, we present a bilinear relationship between M_w and $\log_{10} L$, considering the transition regime of L between 45 and 55 km (in the range adopted by Leonard, 2010). Here, L scales with slope ~0.6 for $M_w \leq 7.1$ and with slope ~0.9 for $M_w > 7.1$. This bilinear relationship is similar to that formu-

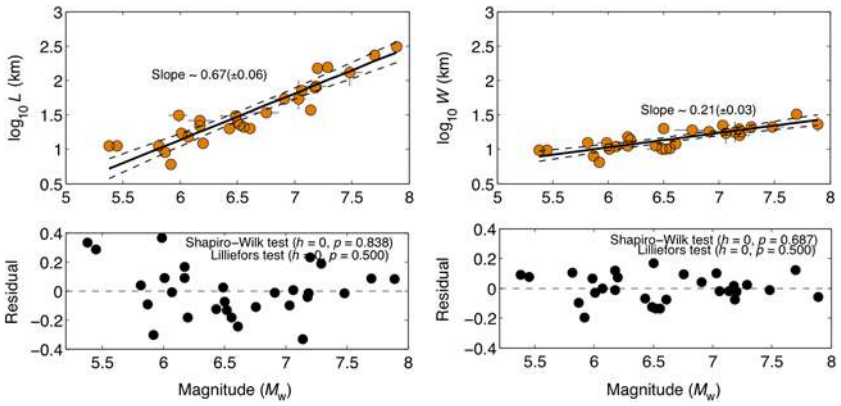

Figure A1. The top panel plots the regression analysis between M_w and $\log_{10} L$, and between M_w and $\log_{10} W$, using the entire dataset of 30 continental strike-slip events with 65 rupture models, covering M_w 5.5–8.0, $L = 6.5$–200 km, and $W = 6.5$–32.0 km. The bottom panel shows the distribution of residuals. The statistical tests for normality, as annotated on each plot, support that the residuals are normally distributed. The color version of this figure is available only in the electronic edition.

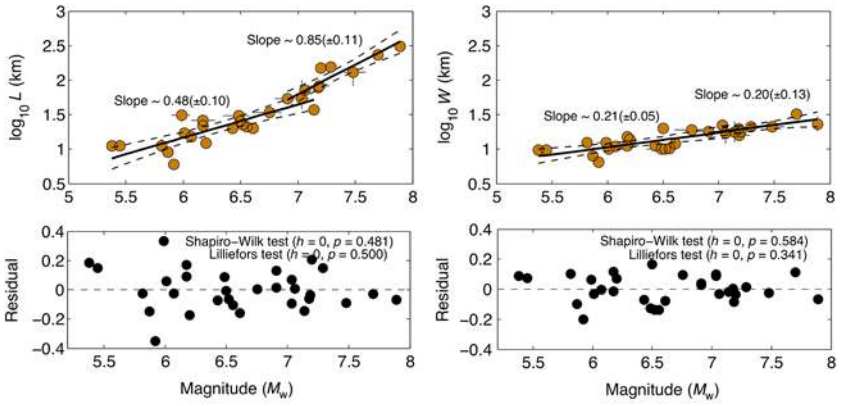

Figure A2. Similar to Figure A1, but now the regression analysis adopts a bilinear model with a crossover at $L = 55$ km between M_w and $\log_{10} L$ and at $L = 45$ km between M_w and $\log_{10} W$. In the case of M_w versus $\log_{10} L$, the slope changes from ~0.6 for $M_w \leq 7.1$ to ~0.9 for $M_w > 7.1$. On the other hand, the scaling relationships between M_w and $\log_{10} W$ have slopes that do not differ statistically and also from the fit on the entire data range (Fig. A1). The bilinear model (specifically for scaling of L) associates a marginally lower average residual but more parameters. Therefore, we cannot conclude it to be better than the linear model. The color version of this figure is available only in the electronic edition.

lated by Leonard (2010). However, regression between M_w and $\log_{10} W$ negates the constant rupture width for $M_w > 7.1$. Instead, it shows a gradual growth of W with increasing M_w. The residuals given by the bilinear regressions do not exhibit any systematic trends. The distributions of residuals in Figures A1 and A2 do not allow discriminating statistically which of the two models is superior.

Nevertheless, we find no evidence that W saturates with increasing M_w, and therefore we favor the linear relationships over the bilinear ones to describe the source-scaling properties of large strike-slip ($M_w \geq 5.5$) earthquakes. Blaser *et al.* (2010) made similar observations based on a different dataset. Additionally, empirical evidence and numerical simulations suggest that W may extend below the locking depth of the fault (Shaw and Scholz, 2001; Jiang and Lapusta, 2016).

Division of Physical Science & Engineering
King Abdullah University of Science & Technology
3114, Building
Thuwal 23955-6900
Kingdom of Saudi Arabia
k.thingbaijam@kaust.edu.sa
martin.mai@kaust.edu.sa
(K.K.S.T., P.M.M.)

Department of Civil Engineering
University of Bristol
Queen's Building, University Walk
Clifton BS8 1TH
United Kingdom
katsu.goda@bristol.ac.uk
(K.G.)

Manuscript received 14 January 2017;
Published Online 25 September 2017